Accepted for publication in: IEEE Open Journal of the Communications Society, March 2026.

IEEE Open Journal of the Communications Society

Received Dec. 23, 2025; revised Mar. 1, 2026; accepted Mar. 5, 2026;
Date of publication MM DD, 2026; date of current version Mar. 10, 2026.

*Digital Object Identifier 10.1109/OJCOMS.2026.XXXXXXX*

# Passive Intelligent Reflecting Surfaces for Efficient 6G mmWave Networks: Design, Validation, and Field Trials

**SIMON HÄGER [1], JOÃO FERREIRA [2,3], STEFAN BÖCKER [1], DOMINIQUE SCHREURS [3], AND CHRISTIAN WIETFELD [1]**

[1]Chair of Communication Networks (ComNets), TU Dortmund University, 44227 Dortmund, NRW, Germany
[2]Keysight Technologies Belgium BV in Rotselaar 3110, Belgium
[3]Division WaveCoRE, Department of Electrical Engineering, KU Leuven, Leuven 3001, Belgium

CORRESPONDING AUTHOR: Simon Häger (e-mail: simon.haeger@tu-dortmund.de).

This work has been partially funded by the German Federal Ministry of Research, Technology and Space (BMFTR) in the course of the *6GEM* research hub under the grant 16KISK038, the *6GEM+* transfer hub under the grant 16KIS2412, and the *PANGOLIN Networks* project under the grant 16KIS2357, by the European Union's Horizon Research and Innovation Program HORIZON-JU-SNS-2022 in the course of the *6G-SANDBOX* project under the grant 101096328, and by the European Union's Horizon Europe Marie Skłodowska-Curie Actions Doctoral Networks HORIZON-MSCA-2022-DN-01 in the course of the *MiFuture* project under the grant 101119643.

**ABSTRACT** 6G millimeter-wave (mmWave) communication systems aim to provide high-capacity networks that span larger areas than before. Particularly, obstacle-induced blockages leading to underconnected non-line-of-sight (NLOS) regions shall be mitigated with cost- and energy-efficient intelligent reflecting surfaces (IRSs) mounted at strategic positions. Static IRSs are particularly promising because they may be realized entirely passively, scaled more easily, incur less implementation loss, and integrated without control signaling. However, they must be deployed with scenario-tailored reflection characteristics. Against this background, this article first presents a holistic beam shaping approach for *HELIOS* IRS geometries, allowing for directed reflection patterns with pre-determined beamwidths and in-beam gains. The analytic model-driven investigation reveals that the changes of module tilt parameters, surface dimensions, and module arrangement successfully deliver quality of service (QoS)-compliant IRSs with little loss against the theoretical performance bound. We then conduct a cross-validation through laboratory measurements and electromagnetic (EM) simulations, which confirm the targeted far-field (FF) performance. The findings also attest good signal integrity and specular suppression characteristics that are better than that of external IRSs. An urban outdoor trial with commercial mmWave devices shows that NLOS user equipment (UE) connectivity stabilizes, with more than 10 dB improvements in both received and transmit power levels as beam management adopts the introduced reflection path. Consequently, throughput enhances by up to 275 Mbit/s.

**INDEX TERMS** Beam shaping, customization, entirely passive, field experiments, intelligent reflecting surface, millimeter-wave communications, radar cross section, 6G.

## I. MOTIVATION: ENHANCING NLOS CONNECTIVITY IN 6G MMWAVE NETWORKS WITH SUSTAINABLE IRSs

THE next generations of mobile radio networks, such as 6G, are expected to expand broadly to higher frequencies than being contained in the traditional sub-6 GHz spectrum. Particularly, frequency ranges 2 and 3 (FR2, FR3), ranging from 7 GHz to 71 GHz and majorly composed of the millimeter-wave (mmWave) spectrum, are expected to alleviate congestion in the limited sub-6 GHz spectrum. This is because the mmWave spectrum offers many wide bands enabling multi-Gbit/s data rates, which are in turn required to make cellular networks future-proof against the continuous exponential increase of wireless traffic consumption. The availability of these bands stems from the traditional telecommunications mindset that mmWave frequencies are hostile to wireless communications due to high propagation losses. However, a paradigm shift occurred within the last decade and led to the adoption of mmWave/FR2 bands spanning

The associate editor coordinating the review of this manuscript and approving it for publication was Naveed Ul Hassan.

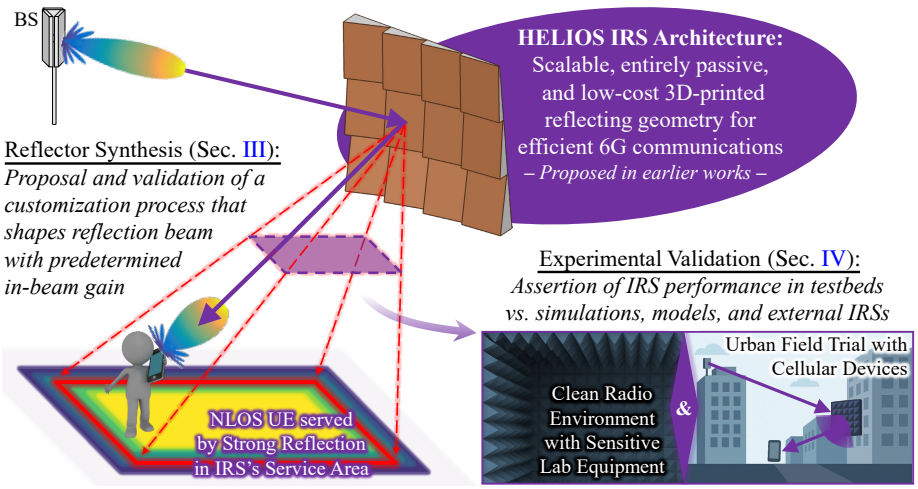


**FIGURE 1.** **This article follows up on our vision of geometry-driven reflectors for efficient 6G mmWave communications, presenting contributions to requirements-compliant IRS beam shaping and experimental performance benchmarking of IRSs.**

24.25 GHz to 71.0 GHz within the 5G New Radio (NR) standard. In this range, large antenna arrays and beamforming transceivers can mitigate the increased free-space path loss, enabling high-throughput line-of-sight (LOS) coverage over distances of up to several kilometers [1]–[4].

The typical outdoor range is nonetheless just a few hundred meters because mmWave base stations (BSs) also face reduced obstacle and vegetation penetration, reduced diffraction, and increased absorption. This results in smaller cell areas and numerous non-line-of-sight (NLOS) zones with insufficient connectivity, especially in dense urban or cluttered industrial settings [5]–[8]. Deploying additional BSs to illuminate these communication blackspots is often prohibitively costly and energy-intensive. To overcome this problem, intelligent reflecting surfaces (IRSs) have emerged as a promising solution: The idea is to reshape the ambient radio environment by redirecting reflections in order to introduce artificial strong propagation paths, either to extend the cell coverage or to increase channel rank within the existing service area. For this purpose, low-cost IRS panels are mounted, for example, on walls in the vicinity of the active radio access network (RAN) infrastructure, to (semi-)passively reflect the incident electromagnetic (EM) wave from the BS to an under-connected region wherein user equipment (UEs) are at a non-specular reflection direction from the IRS. This approach is often summarized by the notion of 6G smart radio environments (SREs) [9]–[11].

There exist numerous types of architectures, such as reconfigurable and static IRSs, transmit and reflect IRSs, as well as active, semi-passive, and passive IRSs [12]–[14]. They are designed to meet different requirements of various use cases, even extending beyond traditional communications. Synthetic reconfigurable intelligent surfaces (RISs), i.e., artificially engineered structures designed to manipulate EM waves in a programmable manner, are the most prominent realization of IRS technology. They offer the advantage of real-time adaptable reflection characteristics enabling flexible use with high impact, but they come at the cost of higher complexity resulting in increased costs, signaling overhead, and insertion loss, moderate energy consumption, as well as reduced scalability of surface size [10], [15], [16]. Owing to numerous challenges that yet need to be addressed, there have been few field trials that have shown successful, albeit only partial, end-to-end integration with real communication equipment [17]–[19]. For these reasons, this article focuses on non-synthetic IRS geometries that obey the natural law of reflection, are non-reconfigurable (i.e., static), and have already been successfully deployed with real communication systems. Specifically, this article investigates so-called *Holistic Enlightening of bLackspots with passIve reflectOr moduleS (HELIOS)* IRSs, see Sec. III-A for details [20]. Similar to other static-passive IRSs [21]–[23], the passive HELIOS panels have been experimentally validated with commercial equipment in private network environments [24]. Their modular, 3D-printed design enables low cost and high scalability, while the naturally static reflection, which is primarily achieved via conductively coated and variably oriented surface patches, eliminates the need for power or signaling.

**Contributions:** With the previous brief background on IRS-assisted 6G mmWave communications, the key contributions of this article, which are shown in Fig. 1 and characterized in detail with respect to the state of the art in Sec. II, are summarized in the following paragraphs:

1) Static-passive IRSs are introduced as a promising enabler for low-cost, entirely passive enhancements of communication services in future 6G networks, supported by reported measurement results, and emerging products. However, current solutions lack optimization procedures that allow them to achieve broad reflections with predetermined reflection gain. This capability is crucial for their integration into network planning frameworks with IRS support, yielding the optimal IRS for a given mounting position in a deployment scenario, thereby realizing an

SRE the assures reliable user application experience. To address this gap, this article proposes and systematically evaluates the performance of the holistic model-driven customization procedure for HELIOS IRSs. Our approach identifies suitable reflector geometries by adjusting module tilt angles, footprint size, and module arrangement. The resulting synthesized IRSs ensure that the target gain is consistently achieved across the entire desired angular reflection space.

2) Much of the existing research on IRSs is simulation- and model-driven, with limited experimental validation. To address this, comprehensive lab and field measurement campaigns are conducted with four custom HELIOS IRSs, systematically validating our model-driven design process against both EM simulations and real-world performance. The investigation span experiments in an anechoic chamber for clean characterization across the full FR2 spectrum as well as urban outdoor trials in pan-European testbeds with commercial equipment, thereby capturing both idealized and realistic propagation conditions. These results not only confirm the proposed IRS design but also provide benchmarking data from reference scenarios that aid ongoing standardization efforts, enable comparisons between IRS platforms, and inform practical 6G deployment strategies. Ultimately, our work delivers an end-to-end validation framework that bridges analytical models, simulations, and experiments, paving the way toward reliable IRS adoption in future networks.

The remainder of this article is organized as follows. Sec. II characterizes our contributions to static-passive IRSs beam shaping, experimental validations of IRSs, and their deployment planning against the state of the art. The HELIOS IRS architecture and the utilized reflection model are first presented in Sec. III. Based thereon, a holistic customization process is proposed and subsequently validated. Sec. IV systematically evaluates the performance of the customized IRSs in both laboratory and field settings and compares them with EM simulations and other IRSs. Finally, Sec. V summarizes the key findings and offers a brief outlook on future work.

## II. STATE OF THE ART: IRS-AIDED COMMUNICATIONS

This section first explores the potential of static-passive IRSs for sustainable future 6G communication networks in Sec. II-A. Sec. II-B then underlines the need for systematic validation of their performance in reference scenarios for standardization purposes. Last, Sec. II-C outlines how this article addresses the previously identified gaps in the state of the art throughout Secs. III to IV.

### A. Potentials of Static-passive IRSs

IRSs are envisioned as a key component of 6G networks, actively shaping the wireless environment to extend coverage, improve pectral and energy efficiency, and reduce interference. Therefore, they promise more reliable and efficient high-throughput communication systems. In particular, they are seen as an enabler for high-frequency communications, for example, in the mmWave/FR2 band. Much of today's research emphasizes reconfigurable IRSs, so-called RISs, which use tunable components to dynamically control amplitude, phase, and pollarization of reflected EM waves. The superposition of numerous individual modules' reflections in the scope of beamforming enables a strong local impact on the radio environment, and therefore, fine-grained optimization of wireless network performance [9], [25, Ch. 9]. Whereas RISs have been a mainstream topic in 6G research, they also face notable drawbacks: their hardware complexity and cost rise with panel size and operating frequency, they suffer implementation losses, and they incur energy consumption [10]. Moreover, along with the need for live optimization in the adaptive reflection beamforming operation mode, they introduce channel estimation and signaling overheads, which can be reduced when instead operating with reflection beam codebook [26]. These challenges motivate the exploration of alternative IRS architectures in contemporary 6G research, such as flexible intelligent metasurfacess (FIMs) which may change their form with movable module positions, e.g., in terms of switching between a flat or curved surface and between uniform and non-uniform module spacings, to dynamically improve its efficiency by matching the IRS geometry to the current deployment scenario [27].

In contrast, static IRSs were long regarded as intermediate solutions on the path toward reconfigurable IRSs, mainly serving as proof-of-concept deployments to validate the benefits of controlling the radio environment [10], [28]. However, they have the advantage of being compatible with current-generation networks [24]. Field trials of such prototypes showcased excellent reflection capabilities in the desired direction [21], [22], [29]–[32]. Emerging products at lower prices compared to RISs further underline the potential of static reflectors [33]–[35]. Particularly interesting are entirely passive, static IRSs, so-called static-passive IRSs, which do not require a power supply, such that the reflector simply needs to be mounted, i.e., neither requiring the development of electrical connections nor regular maintenance operations for battery replacements. Hence, even lower costs can be attained while also improving the RAN's sustainability characteristics. This work follows the above principles and, in contrast to typical synthetic IRSs, employs the natural law of reflection. In a sense, metallic objects of arbitrary shapes typically only opportunistically introduce strong reflection paths in urban outdoor or indoor factory environments as in [8], [36], [37], whereas our concept aims to deliberately introduce such reflecting geometries. In particular, the HELIOS reflector (cf. Sec. III) is a 3D-printed modular geometry which is coated with a conductive varnish to procure high reflectivity. Against this background, this non-synthetic static-passive IRS architecture benefits from even lower production costs and exhibits increased scalability as a contribution to future communication systems.

One drawback of static-passive reflectors compared to RISs is reduced suitability for 6G sensing and positioning services as well as for 6G communication services with movable antenna systems [38]; however, these will need time to establish themselves after the introduction of 6G. In the meantime, static-passive IRSs focusing on 6G communications services will at least drive the short-term success of IRS technology. The key drawback, however, is that the pre-configured reflection behavior cannot be dynamically reconfigured after production and deployment. Hence, the reflector needs to be intelligently custom-tailored to the envisioned use case, such that the reflection beam is directed in the correct direction, has sufficient width to cover the envisioned service area, and exhibits the required reflection gain in order for the anomalous reflection path to be compliant with QoS goals. This includes careful surveying of the geometry of the deployment scenario (i.e., angles and distances) because, particularly when using narrow reflection beams, small angular misalignments of the reflector mounting may induce loss (cf. measurements in [39]). It may also mean that in order to replace a reconfigurable IRS by static reflectors, a larger aperture or multiple reflectors may be needed to efficiently compensate beam broadening-based loss (cf. computational study in [40] or trial in [41]). For this reason, and constituting one of the core contributions of the present work, a static-passive reflector (such as the employed HELIOS architecture) is called an IRS when it is explicitly optimized for its wireless network deployment scenario [28], [29], [42], [43].

Owing to the high number of parameters that need to be set correctly, genetic algorithms (GAs) are commonly used for IRS beam thesis [44], i.e., the optimization of IRSs, for example, to beamform the reflection to a single user [45] as well as multiple users [46]. However, to serve potentially large service areas with static reflectors, the optimization process must also be capable of synthesizing broad beams, which results in a reduction of reflection gain [47]. The works [48]–[50] have realized this for antenna arrays, and the authors in [51] for a mechanical reflect-array, thus underlining that IRS beam broadening should be possible with GAs, as corroborated in [52], [53]. Our previous work has briefly confirmed the feasibility of this approach for geometry-defined IRSs; however, reliance on EM simulations was prohibitive [42]. Hence, we recently presented an analytical reflection model to reduce the long computing time of a single reflection pattern by at least three orders of magnitude, such that thousands of reflection pattern computations within the scope of GA-driven optimization become feasible [54]. Besides the selection of the optimization algorithm, reflector customization heavily depends on the problem formulation. An intuitive approach is to maximize the mean in-beam gain [42] or the integral of reflected energy in the service area [52]. However, this does not necessarily guarantee a certain minimum reflection gain at each angle in the reflection beam. It is therefore important from a network planning perspective, that the custom-tailored IRSs indeed provide the required reflection gain to illuminate the full NLOS region to the level it ought to be for the envisioned use case [55], [56]. *Against this background, Sec. III-A proposes a model-based and GA-driven customization design process for geometric IRSs that are shaped such that (i) the desired reflection gain is guaranteed in the target reflection beam space, while also* (ii) *minimizing the IRS panel size and selecting the most suitable number of reflecting modules.* The dynamic selection of the IRS size and module arrangement, along with the focus on realizing broad reflections, is a contribution to the state of the art, which mostly focuses on narrow pencil beam-like reflections and scaling their gain by adding more IRS panels.

*After proposing the novel customization methodology, a key follow-up contribution of Sec. III-B is the systematic evaluation of its IRS beam shaping capabilities, thereby providing a validated framework applicable to both planning and operation of mmWave networks.* Unlike related works, which at best evaluate the optimization objective, such as the in-beam reflection gain, for a limited set of configurations [28], [32], [43], [45], [52], [53], [57]–[60], this work examines the performance of more than 1,000 synthesized IRSs across beamwidth, IRS panel size, and frequency, and benchmarks against theoretical limits and brute-force solutions. This enables a quantitative evaluation of how closely the designs approach fundamental limits and offers a blueprint for comprehensive beam shaping characterization for IRS-enabled 6G communication.

### B. Importance of Experimental IRS Validation

Years ago, IRSs have been identified as a key enabler to effectively overcome the propagation challenges of high-frequency communication. This has sparked a more than five-year-long gold rush in 6G research, with thousands of papers contributing different aspects to its technology potential. However, most studies are utilizing only analytical model- or simulation-driven methodologies, with a comparably small percentage of literature conducting lab or field experiments with IRSs, as surveyed in [10]. For this reason, using terminology from the Gartner hype cycle [61], the (probably inflated) high expectations for the IRS technology are diminishing into the so-called trough of disillusionment: There are new and existing challenges yet to be addressed, considering there are too few IRS prototypes with a proven track record [10], [62], [63].

Real-world experimental validation is critical to underscore the long-term potential of IRSs, in particular, because propagation characteristics, hardware constraints, and deployment challenges cannot be fully captured through EM simulation alone [64]. Again in the context of the hype cycle, experimental validation of IRSs is essential for progressing toward the so-called slope of enlightment: Based on the experimental insights gained, models can be refined, feasible use cases identified, and the maturity level of selected IRS architectures and design approaches confirmed, thereby facilitating informed expectations about the technology's potential and readiness for market adoption.

This has prompted increasing interest from academia, telecommunication companies, and standardization bodies, including 3GPP and ETSI, to better understand the behavior of IRS-enhanced channels under realistic conditions [65]–[70]. There is currently insufficient agreement on how to model IRSs in the radio channel, especially for passive designs. Like other recent systematic measurements, our own measurement data directly support creating realistic channel models and link-level expectations, aiding standardization efforts [71]–[73]. Furthermore, by systematic measurements of key performance indicators within predefined reference scenarios, better comparability between IRSs is attained, thus allowing for better gauging of the global IRS technology readiness for use in future 6G. *In this context, this work contributes directly to this by a comprehensive lab and field measurements-driven investigation in pan-European testbeds for mmWave IRSs in Sec. IV, which additionally confirms our proposed and analytically validated design process from Sec. III.*

The key aspects motivating the measurement campaigns are provided in more detail, along with the respective contributions, in the following paragraphs:

- **Experimental validation of proposed HELIOS IRS design process:** The HELIOS reflectors are custom-designed to exhibit specific far-field (FF) reflection behaviors based on our contribution in Sec. III. Therein, we systematically validate the performance of the proposed optimization process, which is based on an analytical model to procure QoS-compliant bistatic radar cross section (RCS) patterns in terms of reflection direction, beamwidths, and gain with the smallest possible IRS size and optimal module arrangement. Our contribution in Sec. IV-A is the use of the proposed process to determine IRS geometry blueprints, which are then utilized to manufacture the reflecting geometries. Additionally, a comparison to FF EM simulations is conducted to confirm the desired reflection behavior. Sec. IV-B to Sec. IV-E, as described in subsequent paragraphs, then perform detailed near-field (NF) and FF measurements, and thus comprehensively trial whether the physical implementations deliver the intended performance observable via key wireless communication system metrics. The observed agreement between simulations and measurements supports the use of the analytical design methodology for future real-world deployments. Hence, this work contributes an end-to-end validation of an IRS design methodology based on an analytical model, simulation, and measurement.
- **IRS characterization in clean radio environment with sensitive equipment:** Angular reflection patterns of diverse HELIOS IRSs have already been briefly investigated in a small-scale environment in terms of received power level of a single polarization. However, reflection paths (e.g., from ground and ceiling) could not be fully suppressed, the incident EM wave on the IRS was not planar owing to short distance, and manual movements of the receiver antenna along the circular arc were error-prone [42]. Against that background, this article moves into a large-scale anechoic chamber, which fully suppresses ambient multipath propagation, employs a compact antenna test range (CATR) reflector to realize a realistic impinging EM wave, and features a mechanical turntable for systematic sampling of the angular reflection profile. Moreover, link strength measurements are now conducted for dual-polarized signals and further complemented by signal quality measurements with state-of-the-art measurement equipment. Also, our prior mostly simulations-based assessment of mmWave IRS reflection pattern behavior along the future 6G spectrum [42] is now enriched by measurements across the full licensed FR2 spectrum (24 GHz to 42 GHz). Compliance with methodology in [71], and partially with [72], allows for performance comparisons with other IRSs that are reconfigurable or also static, like HELIOS. Overall, Sec. IV-B to Sec. IV-C contributes a holistic NF reflection characterization for the four reflector prototypes that may serve as a performance reference for other IRSs.
- **Performance benchmarking under realistic propagation conditions:** Whereas theoretical models often assume idealized EM wave propagation and perfect alignment, real deployments involve non-idealities such as diffraction, multipath, polarization mismatch, and mounting tolerances [9], [74]. Even so, trial scenarios like our demonstration of IRS-enabled connectivity for robots in safety cells [24] may be regarded as designed for maximum impact and not reflect typical deployment conditions. Therefore, the field trial of HELIOS reflectors in this work, cf. Sec. IV-D to Sec. IV-E, captures all of the above non-idealities by taking place in an open pan-European test environment. It enables accurate benchmarking of the gain and robustness of HELIOS IRS-based communications in a dense urban environment leveraging time series data of nine channel and link parameters. On the one hand, it is investigated how the availability of pre-configured IRS, in combination with beam management between BS and UE, affects the link strength [75], [76]. Moreover, unlike most studies that focus mainly on using IRSs to extend the coverage [77], the trials in this article examine how IRSs can also reduce power consumption and improve connection reliability on the other hand [17], [78]. These features are becoming more important in the future of 6G, especially for ultra-reliable communications and effective beam management in changing conditions. Like for the lab measurements, direct comparisons with other custom-tailored IRSs that have been measured in the same setup [73] are provided. Our outdoor trial with commercial standalone mmWave communication equipment therefore contributes a report on performance gains across various metrics, thus allowing for better decision making on whether or not to use IRSs to efficiently improve user connectivity in urban street canyons.

### C. Outline of Article Structure

This section briefly describes the structure of the remainder

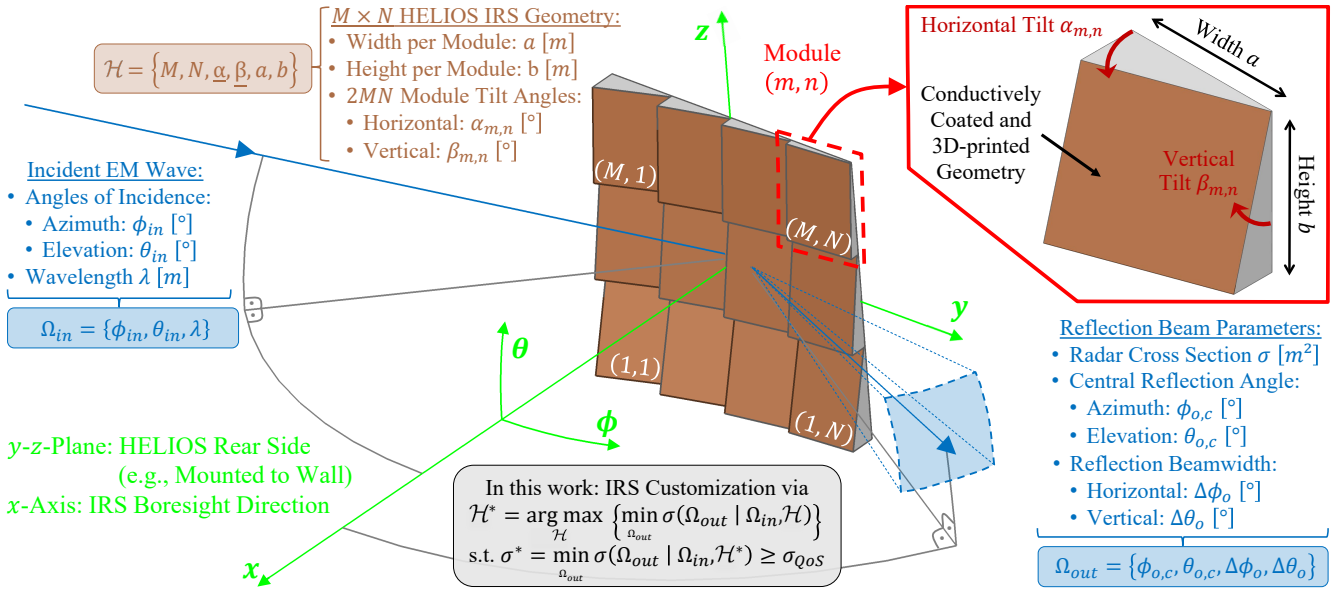


**FIGURE 2.** **Overview of entirely passive, static HELIOS IRS concept [20], depicted for an arbitrarily-selected 3 × 4 geometry. Its parameter set is denoted by $\mathcal{H}$ and optimized such that a custom-tailored deployment in a mmWave network is attained, particularly given the sets of incident wave parameters $\Omega_{in}$ and the desired spatial reflection parameters $\Omega_{out}$ along with the required in-beam gain $\sigma_{QoS}$.**

of the article, which is summarized in Tab. 1 and based on the earlier study of related literature in Secs. II-A to II-B.

According to the motivation in Sec. II-A, Sec. III first proposes a holistic customization approach for HELIOS reflectors, including beam shaping and size optimization capabilities. As a result, reflecting geometries that direct the reflection into the desired angular space with the required reflection gain are attained. The analytical model-driven process is subsequently tested for different beamwidths, sizes, frequencies, and module numbers, as well as assessed against theoretical performance bounds and reference approaches.

We employ our contribution to design and produce four IRSs for experimental assessment in Sec. IV, for which EM simulation results are further considered as a reference. As motivated in Sec. II-B, we conduct extensive lab and field performance measurements of the panels within reproducible and open testbeds as a contribution to standardization activities and improved comparability between existing IRS prototypes. Moreover, the study further confirms our design process and underlines the positive impact of low-cost static-passive IRSs on NLOS user connectivity, thus requiring less signal amplification for both reception and transmission.

**TABLE 1.** **Structure and methodology of remaining article.**

| Sec. | Scope | Data |
|---|---|---|
| III-A | Proposal of holistic HELIOS IRS customization process | – |
| III-B | Sensitivity analysis-driven validation of design process | A |
| IV-A | Model-driven synthesis and simulative pre-assessment of IRSs | A, S |
| IV-B, IV-C | Lab Study: Methodology: CATR chamber, measurement devices; Evaluation of path gains and signal integrity | M, S, A, * |
| IV-D, IV-E | Field Trial: Methodology: Urban scenario, commercial systems; Evaluation with and without IRS for 9 metrics | M, * |

A: Analytical model M: Measurement S: EM simulation *: Comparisons with other IRSs

## III. PROPOSAL AND SYSTEMATIC VALIDATION OF JOINT HELIOS IRS GEOMETRY AND BEAM SHAPING PROCESS

This section first proposes an enhanced reflection model-based design process for geometry-based IRSs in Sec. III-A. It is subsequently systematically characterized in Sec. III-B.

### A. HELIOS Design Methodology

**Adopted reflection model:** A prior customization process incorporated EM simulations that led to a functional, but time-consuming design process [42]. Therefore, it was not feasible to carry out systematic validation for weaknesses. Against this background, we recently introduced a physical optics (PO)-based reflection model for the HELIOS IRS, which was shown to accurately predict its overall bistatic RCS pattern $\sigma(\phi_{out}, \theta_{out})$ with unit $m^2$ (or logarithmically: dBsm) spanning the hemisphere defined by all azimuth and elevation reflection angles $\phi_{out}, \theta_{out} \in [-90°, -90°]$ [54]. Naturally, it requires a parametric description $\Omega_{in}$ of the incident wave, i.e., azimuth and elevation angle of incidence $\phi_{in}, \theta_{in}$, and wavelength $\lambda = c_0/f$, where $c_0$ is the speed of light. Moreover, the following IRS parameters, denoted by $\mathcal{H}$, are considered: module array arrangement $M \times N$, module footprint $b \times a$, and $2MN$ module tilt angles $\alpha_{m,n}, \beta_{m,n}$ with $m = 1, \ldots, M$ and $n = 1, \ldots, N$, as shown in Fig. 2. There is further support for inter-module spacings $d_y, d_z$ and module height offsets $h_{m,n}$ which are not considered in this work for brevity [54].

The analytical reflection model developed for geometry-driven reflectors from [54] is briefly summarized below:

$$\sigma(\phi_{out}, \theta_{out}) = \sum_{m=1}^{M} \sum_{n=1}^{N} \left(\sqrt{\sigma_{m,n}} \cdot e^{j \cdot \psi_{m,n}}\right)^2 \text{ with} \quad (1)$$

$$\sigma_{m,n} = 4\pi \left(\frac{a^r \cdot b^r}{\lambda} \cdot T \cdot \frac{\sin Y}{Y} \cdot \frac{\sin Z}{Z}\right)^2 \text{ using} \quad (2)$$

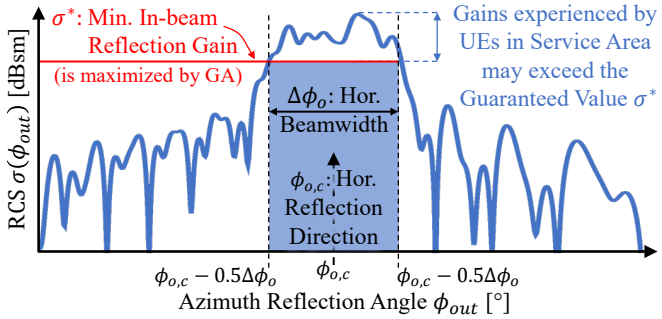


**FIGURE 3.** Extraction of OV $\sigma^*$ from real HELIOS reflection pattern sketched for simplified case of operating in horizontal plane.

$$T = \cos\theta_o^r \sin\theta_i^r \sin\phi_i^r - \cos\theta_i^r \sin\theta_o^r \sin\phi_o^r - \cos\theta_i^r \cos\phi_o^r, \quad (3)$$

$$Y = \frac{\pi \cdot a^r}{\lambda} \cdot \left(\sin\phi_o^r \cos\theta_o^r + \sin\phi_i^r \cos\theta_i^r\right), \text{ and} \quad (4)$$

$$Z = \frac{\pi \cdot b^r}{\lambda} \cdot \left(\sin\theta_o^r + \sin\theta_i^r\right). \quad (5)$$

Moreover, in the equations (2) to (5), the following module-specific geometric transformations are leveraged for brevity:

$$\phi_i^r = \phi_{in} - \alpha_{m,n}, \quad \phi_o^r = \phi_{out} - \alpha_{m,n} \quad (6)$$

$$\theta_i^r = \theta_{in} - \beta_{m,n}, \quad \theta_o^r = \theta_{out} - \beta_{m,n} \quad (7)$$

$$a^r = a \cdot \sqrt{1 + \tan^2\left(\alpha_{m,n}\right)}, \quad b^r = b \cdot \sqrt{1 + \tan^2\left(\beta_{m,n}\right)} \quad (8)$$

In addition, potential self-shadowing between the IRS modules ought to be handled by trimming the surface size $b^r \times a^r$ to the effective reflecting surface patch, as described in detail in [54]. Last, it remains to mention that $\psi_{m,n}$ describes the phase offset between the center of the effective reflecting surface of module $(m,n)$ and the IRS origin.

**Scope of Optimization:** The goal of the IRS design process is to identify a suitable reflector geometry that steers the reflection in a well-defined target reflection area $\Omega_{out}$. This discrete angular range of interest is defined by

$$\begin{aligned}\Omega_{out} = \Big\{(\phi_{out}, \theta_{out}) \in \mathbb{R}^2 \mid \ldots \\ \phi_{out} = \left[\phi_{o,c} - \frac{\Delta\phi_o}{2} : \Delta\phi_{o,res} : \phi_{o,c} + \frac{\Delta\phi_o}{2}\right], \\ \theta_{out} = \left[\theta_{o,c} - \frac{\Delta\theta_o}{2} : \Delta\theta_{o,res} : \theta_{o,c} + \frac{\Delta\theta_o}{2}\right] \\ \Big\} \subset [-90°, 90°] \times [-90°, 90°], \end{aligned} \quad (9)$$

where $(\phi_{o,c}, \theta_{o,c})$ describes the central reflection directions (azimuth, elevation) and $(\Delta\phi_o, \Delta\theta_o)$ defines the reflection beamwidths (horizontal, vertical). Furthermore, this is dependent on the spatial resolution of the reflection pattern, i.e., $\Delta\phi_{o,res}$ and $\Delta\theta_{o,res}$. Whereas our prior work [42] successfully maximized the mean RCS in $\Omega_{out}$, various nulls emerged in the reflection area such that connectivity QoS targets cannot be guaranteed in the target area. Against this background, it is proposed to instead maximize the objective function (OF)

$$\psi\left(\Omega_{out}\right) = \min\ \sigma\left(\Omega_{out}\right). \quad (10)$$

When attaining the peak OV

$$\sigma^* = \max\ \psi\left(\Omega_{out}\right) \quad (11)$$

by the end of the max-min-optimization, UEs in the far field of the IRS and in any direction $(\phi_{out}, \theta_{out})$ contained in $\Omega_{out}$ are guaranteed to be served with a reflection gain, i.e., RCS value of $\sigma^*$ or higher, see Fig. 3. Consequently, a custom IRS that is designed to meet a target gain $\sigma_{QoS}$ provided by network planning, cf. [55], will exhibit an excess gain which is beneficial for the communication link, i.e., it holds

$$\sigma\left(\phi_{out}, \theta_{out}\right) \geq \sigma^* \geq \sigma_{QoS}\ \forall\left(\phi_{out}, \theta_{out}\right) \in \Omega_{out}. \quad (12)$$

To realize this, an alternating optimization (AO)-driven [79], holistic IRS design process is proposed, as depicted in Fig. 4. In the subsequent paragraphs, we first describe the inner part realizing the reflection beam shaping. This is followed up by details on the outer part that conducts the panel size adaptation.

**Joint Reflection Beam and Geometry Shaping:** The optimization in this work assumes a uniform IRS with $M \cdot b$ height and $N \cdot a$ width, i.e., it consists of $M$ rows and $N$ columns of reflecting elements, each with a footprint of $b \times a$, Because each module is described by two tilt parameters, the optimal geometry depends on a large number of parameters $(K = 2 \cdot N \cdot M)$. Therefore, a GA is employed again with the rounded population sizes of $\lfloor 12.5K \rceil$, owing to its suitability for multivariate optimization [80, Ch. 1]. Considering the natural law of reflection for tilted surfaces [20], sensible continuous parameter ranges for $\alpha$ and $\beta$ are determined using

$$\phi_{out} = -\phi_{in} + 2\alpha \text{ and } \theta_{out} = -\theta_{in} + 2\beta. \quad (13)$$

To foster constructive interference between the reflections of the individual HELIOS modules, the following parameter ranges with 25 % additional headroom on either side are used:

$$\alpha_{m,n} \in \alpha_{range} = \left[\frac{\phi_{in} + \phi_{o,c}}{2} \mp \frac{\Delta\phi_o}{4} \cdot (1 + 0.25)\right] \text{ and}$$

$$\beta_{m,n} \in \beta_{range} = \left[\frac{\theta_{in} + \theta_{o,c}}{2} \mp \frac{\Delta\theta_o}{4} \cdot (1 + 0.25)\right] \subset \mathbb{R}. \quad (14)$$

In this context, the *unconstrained* IRS customization process is described by the following optimization problem:

$$\left\{\alpha_{1,1}^*, \ldots, \alpha_{M,N}^*, \beta_{1,1}^*, \ldots, \beta_{M,N}^*\right\} = \arg\max \sigma^*, \quad (15)$$

bounded with respect to (14) and given the deployment scenario parameters $\Omega_{in} = \{\phi_{in}, \phi_{out}, \lambda\}$, IRS architectural

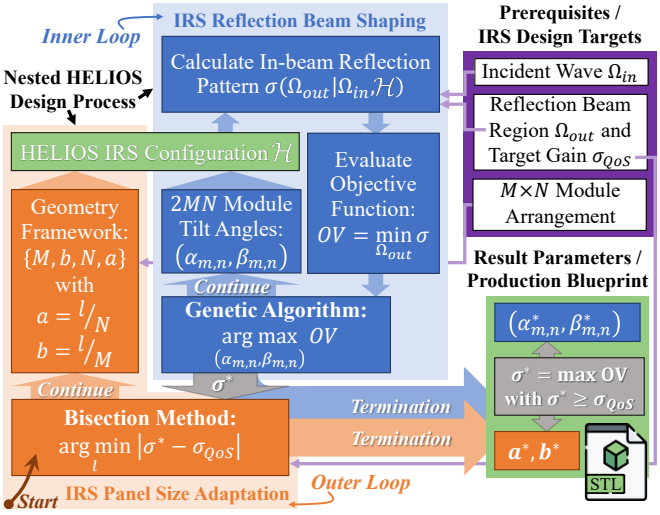


**FIGURE 4.** Overview of proposed $M \times N$ HELIOS IRS customization featuring an alternating optimization approach for joint reflection beam shaping and reflector size adaptation components.

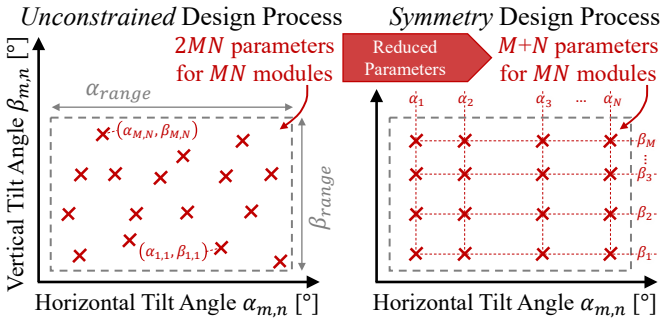


**FIGURE 5.** **Proposed use of *(right)* symmetry conditions between 3D tilts of modules in same row and column to improve performance over the *(left)* unconstrained approach requiring identification of more parameters.**

constraints $\{a, b, M, n\} \subset \mathcal{H}$, and desired reflection characteristics $\boldsymbol{\Omega}_{out} = \{\phi_{o,c}, \theta_{o,c}, \Delta\phi_o, \Delta\theta_o\}$ (cf. Fig. 2). The GA solver stops the optimization process once it cannot improve the OV by at least $10^{-6}$ dB within the last 50 generations.

We subsequently propose to enforce *symmetry* conditions to reduce the number of parameters down to $K = N + M$ (cf. $K = 2 \cdot N \cdot M$ for the *unconstrained* approach), as shown in Fig. 5. Therefore, all HELIOS modules in row $m$ have the same vertical tilt angle $\beta_m$, whereas all elements in column $n$ have the same horizontal tilt angle $\alpha_n$:

$$\alpha_n = \alpha_{m,n}, \beta_m = \beta_{m,n} \; \forall \; m = 1, \ldots, M, n = 1, \ldots, N. \quad (16)$$

The goal of this measure is to improve the efficiency of the multivariate optimization, i.e., for reduced computation time in conjunction with higher OV.

It is noted that both flavors of the design process, *unconstrained* and *symmetry*, can be repeated for better performance. This is because the GA algorithm is likely to select a local maximum instead of the global maximum owing to the large number of parameters ($K$) that need to be established. The reason why repetitions yield different results lies in the inherent randomness of the employed GA, *(i)* particularly the initial population of the GA (first iteration) contains $\lfloor 12.5K \rceil$ fully random chromosomes, with each chromosome representing an individual HELIOS configuration with $K$ parameters that are referred to as genes. Moreover, in the recombination and mutation phase between iterations of the GA, there are *(ii)* random combinations between promising chromosomes of the prior iterations. *(iii)* Some of these new chromosomes further experience random gene mutations. Hence, this article always employs 25 repetitions from which the best solution is selected.

**Adaptation of IRS Footprint & Module Arrangement:** The prior optimization identifies desirable tilt angles $(\alpha^*_{m,n}, \beta^*_{m,n})$ of the HELIOS modules given a fixed module footprint size $b \times a$ with $b, a \in \mathbb{R}^+$, as well as a fixed module arrangement $M \times N$ with $M, N \in \mathbb{Z}^+$. If the attained OV $\sigma^*$ is insufficient, i.e., less than the target value $\sigma_{QoS}$, one needs to systematically adjust $(M, N, b, a)$ and rerun the optimization.

For instance, increasing $b$ and $a$ will increase the IRS reflecting surface area, such that higher reflection gains can be expected [54]. However, larger module dimensions incur different reflection patterns such that corresponding changes of the module arrangement $M \times N$ may be required at some point [54]. It is also noted that the opposite case may also be desirable, i.e., if $\sigma^* \gg \sigma_{QoS}$, the overall reflector size can be minimized to just barely fulfill the design target for minimal required mounting space, production material consumption, and near-field radius. Implications of parameters $\{M, N, b, a\}$ are therefore studied in Sec. III-B.

The following new systematic approach is proposed to adapt $\sigma^*$ according to design goals: First, the problem complexity is reduced by considering a fixed $M \times N$ configuration of quadratic dimensions $l \times l$ resulting in the uniform module widths $a = \frac{l}{N}$ and heights $b = \frac{l}{M}$. This article employs the bisection root-finding method [81, Ch. 5.6] for the function

$$f(l) = \sigma^* - \sigma_{QoS}. \quad (17)$$

It is applicable for small beamwidths because the in-beam RCS $\sigma^*$ is defined continuously and increases strictly monotonously with the IRS side length $l$, cf. (2). The optimization parameter shall have the sensible lower bound $l_{min} = 5\lambda$ (approx. 5 cm), cf. [54], and the arbitrarily selected upper bound $l_{max} = 100$ cm. The search space shall then be iteratively restricted as shown in Fig. 6. During each iteration of the root-finding, it is necessary to run the previously proposed GA-based design process given the current iteration's IRS size. Therefore, in order to limit the computational overhead, the process is terminated early once a custom-tailored reflector with side length $l^*$ fulfilling $f(l^*) \in [0\,\text{dB}, 0.25\,\text{dB}]$, and thus $\sigma^* \geq \sigma_{QoS}$, is observed. For additional efficiency, the GA-based beam shaping subprocess may be terminated early when using very large reflectors that exceed $\sigma_{QoS}$ by several dB, i.e., if $f(l) \geq 3$ dB in this work. The entire process, as shown in Fig. 4, may then be repeated for different $M \times N$ HELIOS configurations to identify the smallest possible IRS. It is then deemed as a size-optimized and QoS-compliant HELIOS design utilizing an efficient $M \times N$ module arrangement.

Against the previously described concept, it is noted that $\sigma^*$ may also decrease for large $l$ when aiming for large IRS beamwidths when considering a suboptimal module arrangement (cf. later results in context of Figs. 7 and 8). Thus, if both $f(l_{max})$ (first iteration) and $f(l_{min})$ (second iteration)

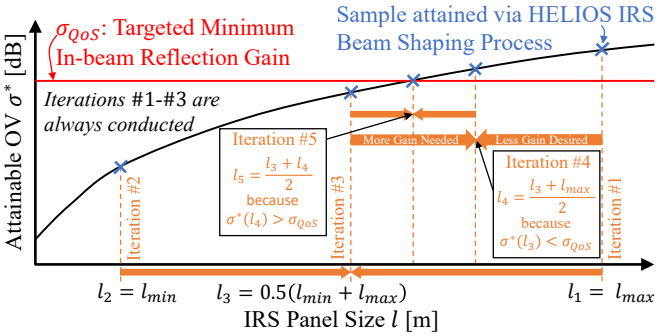


**FIGURE 6.** **Concept for IRS panel size optimization given $\sigma_{QoS}$ performance target. Bisection method adapts IRS size by halving the search space in each iteration until the desired reflection gain is met.**

have a negative sign, the above process would terminate with failure even though there may be a $l \in [l_{min}, l_{max}]$ such that $f(l) = 0$. The above-described non-linear behavior, however, is typically handled by open, i.e., non-bounded root finding methods (e.g., secant method), which are not applicable for our size adaptation problem because, for instance, side length $l$ must be larger than zero. Hence, iteration three is anyway conducted at the midpoint $l_3 = 0.5\,(l_{min} + l_{max})$ such that the bisection method may then be run with the old lower bound $l_{min}$ but new upper bound $l_3$ if the sign of $f(l_3)$ is positive. Similarly, respective fourth and fifth iterations with $l_{3,4} = (0.5 \pm 0.25) \cdot (l_{min} + l_{max})$ may be appended, if necessary. Only if all five cases cannot attain at least $\sigma^* \geq \sigma_{QoS}$, this article deems that the considered $M \times N$ HELIOS IRS cannot attain the desired reflection gain over the given angular beam space, given the predetermined size bounds. As noted before, the full-blown proposed HELIOS design process shall therefore be run for various $M \times N$ IRS module arrangements.

### B. Sensitivity Analysis of Proposed IRS Design Process

This section extensively validates the proposed reflector customization process from Sec. III-A based on the reflection model, because the experimental overhead for this would be too extensive. In the next paragraphs, we present our methodology for the systematic performance study: Performance specifications are introduced first. This is followed by a description of the setup of each validation study, as summarized in Tab. 2. At last, the corresponding results of the three case studies are discussed.

#### 1) Methodology

**Performance Metrics:** To assess the quality of our proposed design process yielding OVs $\sigma^*$, this article considers an upper-bound performance limit $\sigma_{bound}$ for the IRS reflection beam customization process, which is attained as follows: The RCS reflection pattern of a flat perfect conducting plate is leveraged, considering the carrier frequency, azimuth and elevation angles of incidence, angular resolution, and surface side lengths as described later. It is attained via EM simulations with `Ansys HFSS` [82]. The reflection is then numerically integrated over the full reflecting hemisphere and subsequently distributed fairly over the considered angular service area of the IRS to approximate

$$\sigma_{bound} = \frac{1}{\Delta\phi_o \cdot \Delta\theta_o} \cdot \iint_{-90^\circ}^{90^\circ} \sigma\left(\phi_{out}, \theta_{out}\right)\, d\phi_{out}\, d\theta_{out}. \quad (18)$$

It is noted that such an ideal reflection pattern, i.e., constant reflection gain in the service area and no reflection power to outside angular ranges, is physically impossible. Therefore, this article refer to this performance bound as a *theoretical limit*.

The *brute-force* approach requires discretization of the solution space to conduct an exhaustive search to identify the best IRS geometry using the same objective function as our proposed approach. The search spaces $\alpha_{range}$ for horizontal tilt angles $\alpha_{m,n}$ and $\beta_{range}$ for vertical tilt angles $\beta_{m,n}$ are sampled with 0.05° resolution, allowing the scheme to consider beam changes exactly in the order of the employed reflection beam resolution of 0.1°. Owing to high computational load, the brute-force approach is realized for the symmetry-based solution parameter space, requiring identification of just $N+M$ parameters for a $M \times N$ HELIOS, cf. Fig. 5. Nonetheless, as the overhead grows exponentially with the targeted beamwidth, the brute-force solution is only considered for $2 \times 2$ IRSs in this work, where there are, for example, 150 and 510 million configurations to be tested at the beamwidths of 15° and 20°. By assessing the performance of *permutated IRS geometries* that were selected by our proposed design process, this article loosely extends the brute-force performance reference to reflectors with much higher module numbers. In total, there are $(M!) \cdot (N!) - 1$ permutated geometries that are assessed per custom-tailored IRS when considering symmetry-based HELIOS designs, i.e., up to 575 for $M = N = 4$. In this work, this metric is employed to assess whether the design process has a high or low likelihood of selecting a local optimum.

**Setup of Validation Case Studies:** Three analytical reflection model-driven case studies are conducted, typically employing the following common set of parameters, cf. Tab. 2:

- 27.1 GHz carrier (3GPP mmWave band n257),
- Angles of incidence: $\phi_{in} = -45^\circ, \theta_{in} = 0^\circ$,
- Center reflection direction: $\phi_{o,c} = 45^\circ, \theta_{o,c} = 0^\circ$,
- Angular resolution: $\Delta\phi_{o,res} = \Delta\theta_{o,res} = 0.1^\circ$,
- $M \times N$ HELIOS with $M = N = 1, 2, \ldots, 6$, and
- Process variants: $\{unconstrained, symmetry\}$.

This scenario clearly does not require a change of the reflection angle to serve the center reflection direction. This was already realized and experimentally validated in [20], [83], however, the capability to change the center reflection direction will again be demonstrated experimentally in Secs. IV-C and IV-E. Considering the above-described situation ($\phi_{o,c} = -\phi_{in}, \theta_{o,c} = -\theta_{in}$), and when aiming for a narrow reflection ($\Delta\phi_o, \Delta\theta_o \to 0^\circ$), one would *expect a perfect flat plate*, i.e., $\alpha_{m,n} = \beta_{m,n} = 0^\circ$ for all modules $(m, n)$ regardless of the considered number of reflecting modules $M \cdot N$. Depending on beamwidth, one could also *expect a concave geometry* [20]. These expectations are therefore asserted in the evaluation.

The *first case study*[1] focuses on assessing the proposed schemes' ability to synthesize broad reflection beams with a squared beam shape in angular space using beamwidths $\Delta\phi_o = \Delta\theta_o = 1^\circ, 2^\circ, \ldots, 25^\circ$. For that reason, a fixed reflector size of $l = M \cdot b = N \cdot a = 0.5\,\text{m}$ is leveraged. Against that background, the performance of the two proposed flavors, particularly in terms of attained OV $\sigma^*$, is compared directly, factoring in different beamwidths and numbers of HELIOS modules with $M = N = 1, 2, \ldots, 6$. Furthermore, the performance is characterized against a theoretical limit, which was introduced previously in the context of (18). Additionally, comparisons are made against the performance

[1] Please note that these custom-tailored static IRSs are also used to study the impact of beam misalignments, given in the Appendix.

**TABLE 2. Overview of computing parameters throughout sensitivity analysis of the proposed HELIOS IRS optimization scheme, with case studies #1–#2 focusing on IRS reflection beam shaping and case study #3 on IRS panel size adaptation.**

| | Parameter | Description/Value |
|---|---|---|
| Common | Angles of Incidence | $\phi_{in} = -45°$, $\theta_{in} = 0°$ |
| | Center Angles of Departure | $\phi_{o,c} = 45°$, $\theta_{o,c} = 0°$ |
| | Angular Resolution | $\Delta\phi_{o,res} = \Delta\theta_{o,res} = 0.1°$ |
| | Module Tilt Angles | $\{\alpha_{1,1}, \ldots, \alpha_{M,N}, \beta_{1,1}, \ldots, \beta_{M,N}\}$ flexible with (14) |
| Case Study #1 | Carrier Frequency | $f = 27.1\,\text{GHz}$ |
| | Reflector Footprint | $M \cdot b = N \cdot a = 50\,\text{cm}$ |
| | 6 Module Arrangements | $M = N = 1, 2, \ldots, 6$ |
| | 25 Reflection Beamwidths | $\Delta\phi_o = \Delta\theta_o = 1°, 2°, \ldots, 25°$ |
| | 2 Process Variants | *symmetry*, *unconstrained* |
| | Reference Solutions | Theoretical Limit, Brute-force, Result Permutations |
| | → Results depicted in: Fig. 7, Figs. 9a to 9c | |
| Case Study #2 | Carrier Frequency | $f = 27.1\,\text{GHz}$ |
| | 46 Reflector Footprints | $M \cdot b = N \cdot a = 10\,\text{cm}, 12\,\text{cm}, \ldots, 100\,\text{cm}$ |
| | 6 Module Arrangements | $M = N = 1, 2, \ldots, 6$ |
| | Reflection Beamwidth | $\Delta\phi_o = \Delta\theta_o = 10°$ |
| | 2 Process Variants | *symmetry*, *unconstrained* |
| | Reference Solutions | Theoretical Limit, Result Permutations |
| | → Results depicted in: Fig. 8, Fig. 9d | |
| Case Study #3 | 3 Carrier Frequencies | $f = 3.7\,\text{GHz}, 15.0\,\text{GHz}, 27.1\,\text{GHz}$ |
| | Reflector Footprints | $l = M \cdot b = N \cdot a$ flexible with $l \in [5\,\text{cm}, 100\,\text{cm}]$ |
| | 10 Module Arrangements | $1 \leq M \leq N = 1, 2, \ldots, 6$ |
| | 2 Desired Beam Shapes | A, B |
| | Reflection Beamwidths | $\Delta\phi_o = \Delta\theta_o = 3°$ (A) *or* $10°$ (B) |
| | Target Gains | $\sigma_{QoS} = 22\,\text{dBsm}$ (A) *or* $12\,\text{dBsm}$ (B) |
| | Process Variant | *symmetry* |
| | → Results depicted in: Tab. 3, Tab. 4 | |

attained using a brute-force approach, however, only for the $2 \times 2$ HELIOS case, owing to computational overhead. By means of assessing whether permutations of the custom-designed HELIOS improve the performance, the brute-force concept is loosely extended to the configurations with up to $5 \times 5$ modules. This allows us to ascertain whether local or global optimization results are identified by the GA. Overall, the first case study bundles the results of 300 custom-tailored IRSs using our proposed design process, with hundreds of millions of more reflection geometries being considered by means of result permutations and the brute-force approach.

In a similar fashion to the above-described study, the *second case study* instead assesses the performance for different reflector sizes ranging from $l = 0.1\,\text{m}$ to $l = 1.0\,\text{m}$ in steps of 2 cm for a fixed beamwidth of 10°. This sensitivity analysis considers six types of $M \times N$ reflectors with $M = N = 1, 2, \ldots, 6$. Again, comparisons between the two flavors of the proposed design process are made and augmented by a characterization of the attained performance against the theoretical limit. Overall, the second case study considers 552 custom-tailored IRSs reflection beams and geometries.

Last, the *third case study* tests the size optimization based on the symmetry-based custom-design process A $2 \times 2$ HELIOS configuration is selected to realize $\sigma_{QoS} = 22\,\text{dBsm}$ over the beamwidths $\Delta\phi_o, \Delta\theta_o = 3°$ at 27.1 GHz. The attained size is compared directly with the result from the first case study, wherein the IRS has a size of $50\,\text{cm} \times 50\,\text{cm}$. Subsequently, the spectrum is switched to 3.7 GHz (in frequency range 1 (FR1)/sub-6 GHz spectrum, licensable for private networks in Germany) and 15.0 GHz (in FR3 candidate spectrum for 6G) to find out how large a HELIOS IRS would need to be in order to deliver the same $\sigma_{QoS}$ for the same $\Omega_{in}$ and $\Omega_{out}$ parameters. To find the smallest possible HELIOS geometry, the full proposed reflector customization process is conducted not just for $2 \times 2$ module arrangements but for ten different $M \times N$ arrangements in total. This study is then repeated for increased beamwidths $\Delta\phi_o, \Delta\theta_o = 10°$ along with the reduced $\sigma_{QoS} = 12.0\,\text{dBsm}$ target, for which a $3 \times 3$ HELIOS configuration from the second case study serves as the reference.

### 2) Results and Discussion

The subsequent paragraphs present and evaluate the results of our three case studies according to the previously described methodology. The sensitivity analysis begins with the *beam broadening capabilities* **(case study #1)** of the proposed reflector design process as presented in Fig. 7.

The evaluation begins by considering the symmetry-based design approach for different beamwidths in Fig. 7a. It can be seen that the performance differs for the different leveraged module arrangements despite utilizing the same IRS size ($N \cdot a = M \cdot b = 50\,\text{cm}$), for example, the single module (1×1) reflector performs well for small beamwidths of up to about 1.5° but fails to realize consistent in-beam gains when targeting larger beamwidths. For beamwidths of up to about 7.5°, a 2×2 HELIOS provides the highest gain. However, similar to the single module reflector, a rapid falloff in OV $\sigma^*$ is observed for higher beamwidths. For a 25° beamwidth, the gap against the $5 \times 5$ configuration exceeds 20 dB. Thereafter, the $3 \times 3$ HELIOS realizes the best guaranteed in-beam RCS level for beamwidths of up to approximately 16.5°. Again, performance drops for higher beamwidths. The novelty here, however, is that this constellation performs worse for small beamwidths than, for example, the 2×2 IRS. These trends can again be observed for the $4 \times 4$ HELIOS, which performs best for beamwidths in the approximate range from 16.5° to 24.5°, but incurs a loss for smaller and larger beamwidths compared to other $M \times N$ arrangements. Using too many modules results in moderate losses of up to 10.4 dB, whereas the use of too few modules results in high losses of several tens of dB. Thus, is is clearly observed that there is an optimal number of modules to be used in order to attain IRSs with the targeted beamwidth along with the maximum corresponding OV $\sigma^*$.

It is now investigated with Fig. 7b how well the symmetry-based design process performs against the unconstrained variant, considering the $M \times N$ module arrangement which maximizes the minimum in-beam gain $\sigma^*$. It appears that the reduced number of parameters in the symmetry-based approach bears fruit for beamwidths of 7° and higher, with the unconstrained approach suffering increasing loss of up to 26.1 dB for 25° broad beams. The starting point for this behavior aligns well with the switch to IRSs with 3×3 modules, resulting in $2 \cdot M \cdot N = 18$ instead of $M + N = 6$ parameters, which makes GA-based selection of the global maximum less likely. Whereas this is a disadvantage for IRSs that need to

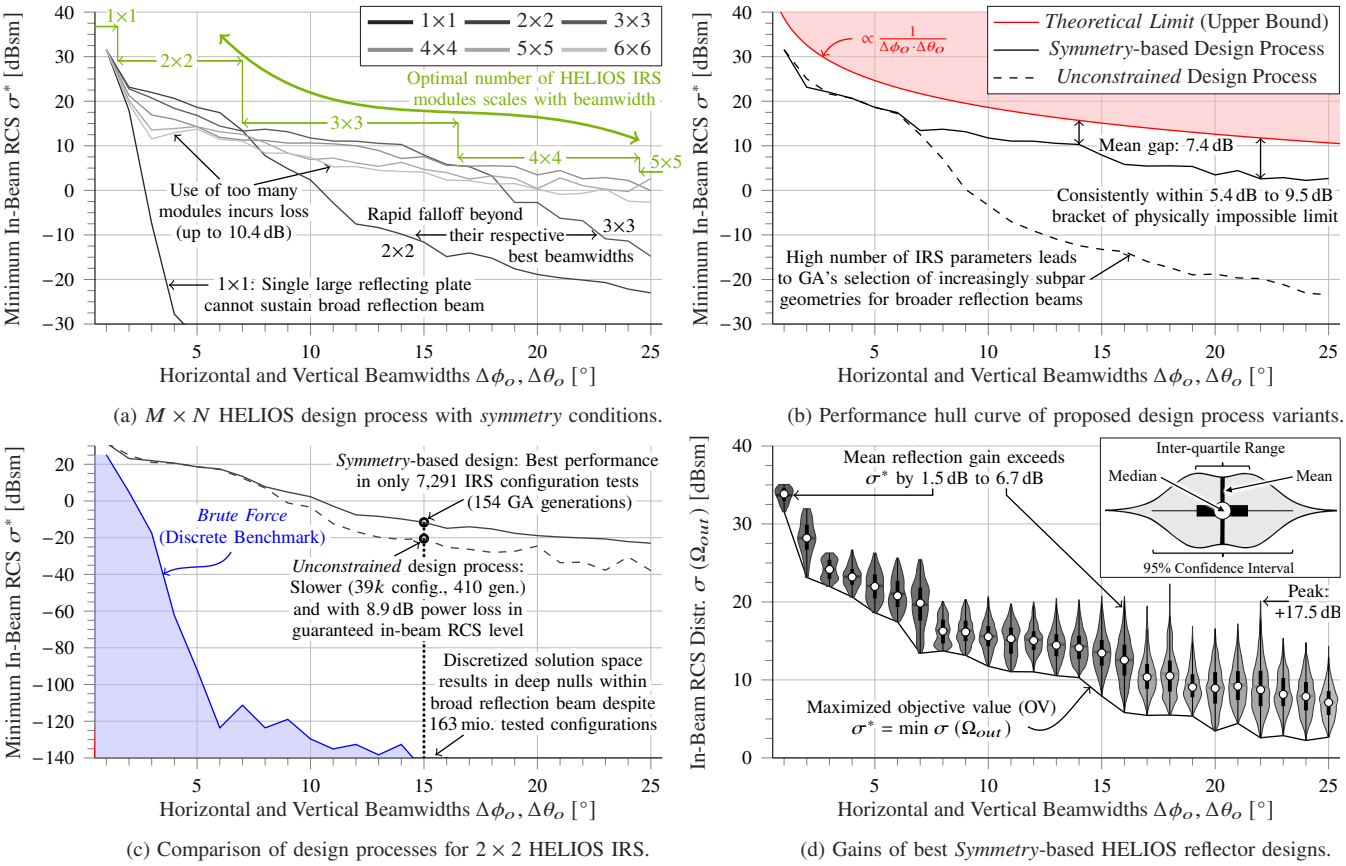


(a) $M \times N$ HELIOS design process with *symmetry* conditions.

(b) Performance hull curve of proposed design process variants.

(c) Comparison of design processes for $2 \times 2$ HELIOS IRS.

(d) Gains of best *Symmetry*-based HELIOS reflector designs.

**FIGURE 7. Sensitivity analysis with respect to targeted beamwidths of the proposed *symmetry*-based HELIOS design process utilizing 0.5 m × 0.5 m IRSs. *(a)* Variation of $M \times N$ module arrangements yield that the optimal module number depends on the beamwidth: few for a narrow reflection, many for broad beams. *(b)* *Symmetry*-driven variant with reduced number of parameters outperforms the *unconstrained* variant for larger beamwidths and remains close to the *theoretical limit*. *(c)* Both design approaches dominate the *brute-force* solution in terms of realized objective value and computational load. *(d)* The in-beam reflection gain is on average 4.4 dB higher than the OV $\sigma^*$, with peak gains of up to 17.5 dB, which opportunistically improve link QoS.**

realize broad reflection beams, narrow reflection beams of 2×2 reflectors can be attained slightly better, cf. higher gain at 2° beamwidth. The lack of high performance for broad beams, which needs to be attained for practical deployment of static IRSs, however, makes the symmetry-based approach the more desirable choice. Particularly, because it can also be extracted from Fig. 7b that its performance consistently remains within the 5.4 dB to 9.5 dB range of the physically impossible to meet theoretical performance limit, which assumes that all reflecting energy is radiated with the same magnitude into the desired beam space and none outside of it. Considering that *(i)* reflections on flat conductive surfaces have strong sidelobes, and thus energy outside the desired angular beam area, as well as *(ii)* the combined reflection of multiple such modules leads to destructive interference, and thus a less efficient energy distribution within the targeted beam area, it is remarkable to find that there is, on average, only a 7.4 dB loss, i.e., the minimum in-beam gain could in theory only be higher by factor 5.5.

Both design flavors ($2 \times 2$ IRS) are now compared against the brute-force approach in Fig. 7c, which has systematically swept the search space (cf. $\alpha_{range}$ and $\beta_{range}$ for horizontal and vertical tilt angles) with 0.05° resolution. It can be seen that this approach drastically deteriorates for larger beamwidths, exhibiting more than 100 dB loss. Naturally, the performance could be better for an even finer resolution. However, considering the already high computational effort, this is no practical solution: For the 15° beamwidth, the provided brute-force solution is based on more than 163 million tested IRS configurations, which is approximately 4,200- and 22,300-times more than the unconstrained and symmetry design process flavors. This gap would widen even more for higher bandwidths as well as for IRSs with even more modules, thus making the brute-force practically infeasible and underlining the usability of our proposed design process.

Having observed for the $2 \times 2$ IRS that brute-force performs poorly in terms of attained performance for the given computational overhead, permutations of the unconstrained and symmetry design process results of up to 16-module IRSs ($2 \times 2 - 4 \times 4$) are considered. Upfront, it is noted that even the best permutated HELIOS configuration typically incurs a loss compared to the geometry selected by the optimization process, for example, −4.1 dB for the symmetry-based design process and −3.0 dB for the unconstrained approach. This is a result of the respective low probabilities of about 2.9 % and 3.6 % that one of the available geometry permutations of the design process yields a better performance. Nonetheless,

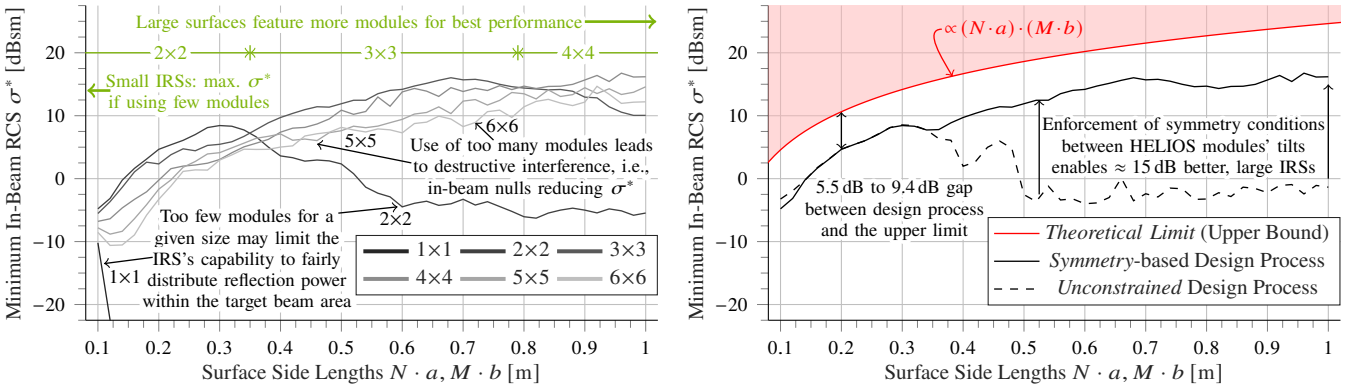


(a) $M \times N$ HELIOS design process with *symmetry* conditions.

(b) Performance hull curve of proposed design process variants.

**FIGURE 8. Sensitivity analysis with respect to IRS sizes of the *symmetry*-based HELIOS design process providing 10° broad beam. *(a)* The optimal module number depends on the overall reflector size: few modules for small reflectors, many for large surfaces. *(b)* Proposed *symmetry* HELIOS design process variant with reduced parameter number again outperforms the *unconstrained* variant for larger IRSs sizes and remains close to the *theoretical limit*.**

permutation-based gains of up to 5.1 dB in OV $\sigma^*$ are possible for the symmetric design process, and up to 12.4 dB for the unconstrained process. All of these metrics again underscore that the use of symmetry conditions yields better performance because the GA is less likely to select a local optimum and, if so, with less loss to the global optimum.

Fig. 7d shows the in-beam RCS distribution of the best IRS designs identified by the symmetry-based design process. The line below the violins is the previously discussed OV $\sigma^*$, which is, by definition (cf. Sec. III-A), the minimum gain of the reflection beam in the designated angular reflection beam area. Considering the mean delta of 1.5 dB to 6.7 dB and peak delta of up to about 17.5 dB over $\sigma^*$, this figure underlines that the HELIOS reflectors will exhibit an excess gain for UEs within the designated target space. If we had maximized the mean in-beam gain instead of the minimum in-beam gain, we would have attained higher OVs at the cost of being unable to provide a minimum service quality to UEs in the designated service area of the IRSs. This would be destructive for private industrial networks requiring service guarantees. Hence, this article chose to guarantee the desired reflection gain and additionally benefit from some opportunistic gains at numerous positions in the custom-tailored beam.

Having observed that reflection gain diminishes proportionally to respective increases in azimuth and elevation bandwidths, it is now assessed whether our proposed design process operates well with other IRS sizes. In particular, one would expect a large-scale IRS to realize higher RCS values than the previously considered 50 cm × 50 cm reflectors. Hence, the loss from beam broadening could be easily compensated. The proposed reflector design process's *scalability in terms of the IRS panel size* **(case study #2)** is thus presented using Fig. 8.

Let us first consider the symmetry-based design approach for different reflector sizes in Fig. 8a. It can be seen that the performance differs for the different leveraged module arrangements despite exhibiting the same beamwidth ($\Delta\phi_o = \Delta\theta_o = 10°$), for example, the four-module (i.e., $2 \times 2$) HELIOS performs well for comparatively small side lengths of up to about 35 cm but fails to realize consistent in-beam gains for larger beamwidths. For side lengths of up to about 79 cm, a $3 \times 3$ HELIOS provides the highest gain. But similar to the $2 \times 2$ IRS, a rapid falloff in OV $\sigma^*$ is observed for larger reflector panels. Thereafter, the $4 \times 4$ HELIOS realizes the best guaranteed in-beam RCS level for side lengths of up to approximately 1 m. Similar to the previous sensitivity analysis to beamwidth (cf. Fig. 7a), Fig. 8a shows clearly that the use of too many modules for a given IRS size results in loss of up to about 10.6 dB. Again, one can also use too few modules given the reflector size: It is not a surprise that a single reflecting surface ($1 \times 1$) is unsuitable for the targeted $10° \times 10°$ beam area, at least for practical surface dimensions where the IRS is not just a pure scatterer ($N \cdot a, M \cdot b \gg \lambda$). Similarly, the $2 \times 2$ and $3 \times 3$ incur losses of up to 17.7 dB. Thus, it has been observed clearly that there is an optimal number of modules to be used in order to attain IRSs of a given size with the maximum corresponding OV $\sigma^*$.

Fig. 8b allows for evaluation of how the symmetry-based design process performs in comparison to the unconstrained variant, considering the respective $M \times N$ module arrangement that maximizes the minimum in-beam gain $\sigma^*$. With similarities to the sensitivity analysis for the desired beamwidth (cf. Fig. 7b), it is found that the reduced number of parameters in the symmetry-based approach yields benefits for IRS panel sizes of 35 cm and larger, with the unconstrained approach suffering an increasing loss of up to 17.2 dB. The starting point for this behavior again aligns well with the switch to IRSs with $3 \times 3$ modules, resulting in 18 instead of 6 parameters, thus making GA-based selection of the global maximum less likely. On the opposite side of things, is can also be observed that the unconstrained variant can yield better results for small IRSs, i.e., smaller than 14 cm, with few modules. Nonetheless, we summarize that the proposed symmetry-based design method is favorable as the deployment of large-scale IRSs is foreseen for 6G networks. Therefore, this article now compares the symmetric HELIOS optimization scheme against the theoretical performance limit in Fig. 8b

to assess how good the attained performance is against the physically impossible to meet upper bound. It can be observed that the loss is consistently in the range of 5.5 dB to 9.4 dB, with a slightly lower mean of 6.8 dB, which aligns well with the prior results in Fig. 7b. In this context, it must be noted that similar to the results observed in Fig. 7d, the IRSs of various size typically attain a mean RCS value that is 4.0 dB above the OV, thereby closing the mean gap to the limit. Again, UEs at oportunistic angles within the reflection beam space may even experience peak gains of up to 15.2 dB over the OV. In contrast, however, is can be noted that there are performance dips compared to the theoretic bound in the regions where the optimal number of modules changes, i.e., for size of about 35 cm and 80 cm. This shows that one could potentially improve the performance in these regions if using $M \times N$ IRSs for which $M \neq N$, for example, the $2 \times 3$ arrangement could be employed to efficiently bridge the transition between the $2 \times 2$ and $3 \times 3$ IRSs with panel side lengths of approximately 35 cm.

To extend on the previous two case studies #1–#2 in the context of Figs. 7 and 8, four selected customized reflecting geometries (with *symmetry*) are considered along with their RCS beam pattern in Fig. 9. It is noted that the geometries are depicted with scaled $x$-axis which makes it easier to detect patterns in the employed module tilt angles: In the top row (i.e., Fig. 9a), we find the single-module, 0.5 m × 0.5 m reflecting surface which attains the maximum OV $\sigma^*$ for a $1° \times 1°$ target beam area, with the main lobe of the reflecting beam being broader than the target region. One can see that the reflector is effectively a flat plate, i.e., tilt angles $\alpha_{1,1}, \beta_{1,1} \approx 0°$, which matches fully with our previously introduced expectations. When broadening the reflection to 4° in azimuth and elevation angle domains, respectively, a $2 \times 2$ HELIOS IRS with a concave form factor is identified by our symmetric custom-tailoring process, see Fig. 9b. The corresponding pattern on the left side exhibits nine main lobes with weak intermittent nulls, thus showcasing that the genetic optimization has successfully tilted the four modules such that main and side lobes of the individual modules' reflection pattern superimpose over the whole target beam area as much constructively as possible. Again, it can be found that there is significant reflection gain outside the desired reflection area, which is a combined effect of allowing 25 % headroom for the $\alpha_{range}$ and $\beta_{range}$ solution spaces on the one hand, and that the GA broadly distributes the tilt angles to mitigate reflection nulls to maximize the OV, as it is defined as the minimum in-beam reflection gain. Thus, it underlines that the employed target beamwidth definition does not adhere to common beamwidth definitions, such as the half-power beamwidth.

Fig. 9c provides the IRS with an even larger beamwidth of 10°, i.e., with a 6.3-times larger target beam area than in Fig. 9b, yet still with side lengths of 0.5 m. This geometry is now based on nine instead of four modules, yet the concave form factor remains. The attained reflection gain in the angular target area has again been reduced, as expected based on the assessment in Fig. 7. However, compared to Figs. 9a and 9b, several small null regions can be observed in the reflection beam. These make it impossible to guarantee, for example, at least 15 dBsm throughout the entire target beam region. Hence, by rerunning the optimization process for a larger IRS footprint like those considered in the context of Fig. 8, this problem can be mitigated. Accordingly, Fig. 9d provides the best $4 \times 4$ HELIOS geometry with a footprint area of 1 $m^2$ along with its reflection pattern. At first glance, the geometry seems to be unrelated to the above depicted geometries. However, if one were to flip the module order both horizontally and vertically, we would again attain a convex module arrangement. Due to testing all permutations of the depicted geometry, is is known that this concave form performs worse; even the best of all 575 trialed permutated geometries exhibits a 0.8 dB reduced OV $\sigma^*$. A reason for this is that the center reflection point of the effective non-self-shadowed reflecting surface of each HELIOS module has a significant impact on constructive and destructive interference between the individual reflection patterns of the modules, and thus, the overall reflection pattern (cf. Sec. III-A and [54]). Hence, the GA has found an

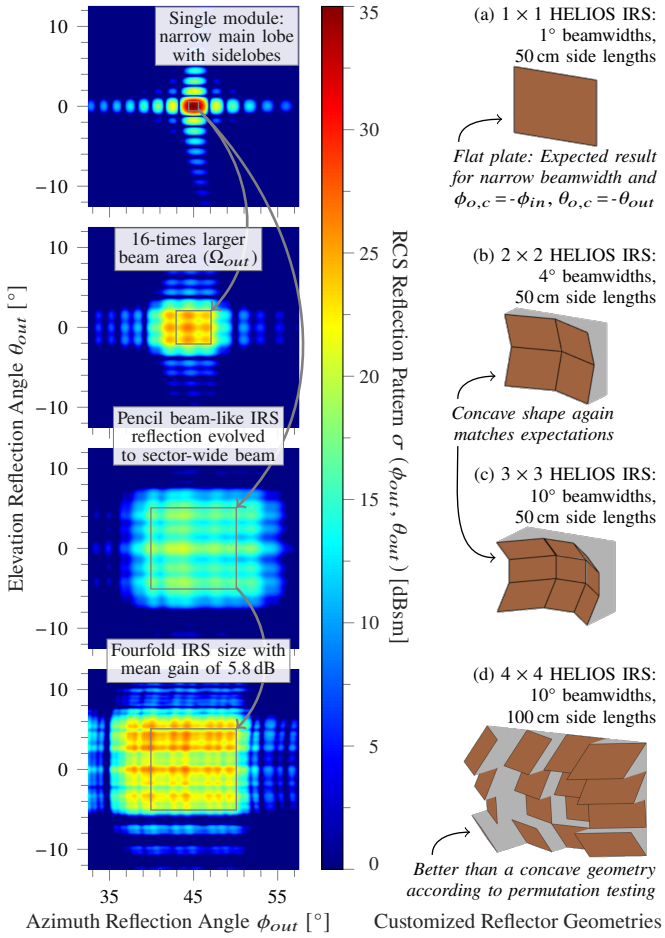


**FIGURE 9. Reflection beam broadening without changing the natural reflection direction: Increasing the target beamwidth from *(a)* to *(c)* reduces in-beam gain, which can be compensated by *(d)* enlarging the IRS size. The validity of the customized HELIOS configurations is particularly evident for small beamwidths and panels, where geometric expectations are met.**

unintuitive but more effective IRS geometry. Importantly, the scaled reflecting geometry in Fig. 9d does not exhibit the null regions from Fig. 9c anymore and can therefore guarantee the previously considered 15 dBsm minimum bistatic RCS target.

Against this background, this article now evaluates in the context of Tab. 3 whether the proposed *IRS size adaptation mechanism* **case study #3** can determine optimally sized, custom-tailored HELIOS IRS geometries that just exceed the reflection strength target $\sigma_{QoS}$ of 22 dBsm, while meeting the reflection beamwidth requirement of 3° in both the azimuth and elevation domains. It is found in the right column for operation at a 27.1 GHz carrier (also used in previous paragraphs) that the smallest HELIOS IRS has the dimensions of 50.27 cm × 50.27 cm, which is attained with a 2×2 module arrangement. It exhibits a small headroom of 0.07 dB over $\sigma_{QoS}$, which is within the tolerated 0.25 dB range for successful termination. Overall, the size adaptation sub-process has considered nine IRS panel sizes for which respective runs of the beam shaping sub-process (with symmetry conditions) were conducted. This custom IRS provided by the full-blown customization process confirms our result from Fig. 7a, wherein a 50 cm×50 cm attained only 21.9 dBsm, i.e., a slight increase in size was to be expected. Given that the 2×2 constellation performed best for the targeted beamwidth in Fig. 7a, larger panel sizes were to be expected for the other $M \times N$ IRSs in Tab. 3.

**TABLE 3.** **Holistic HELIOS IRS customization across 6G bands: Unique size-minimized $M \times N$ reflectors are attained for a *high in-beam gain* ($\sigma_{QoS}$ = 22 dBsm) / *narrow beam area* ($\Delta\phi_o = \Delta\theta_o$ = 3°) design target.**

| | 3.7 GHz (FR1) | | | | 15.0 GHz (FR3) | | | | 27.1 GHz (FR2) | | | |
|---|---|---|---|---|---|---|---|---|---|---|---|---|
| M×N Modules | QoS met? | #Iterations | OV $\sigma^*$ [dBsm] | Size $l^*$ [cm] | QoS met? | #Iterations | OV $\sigma^*$ [dBsm] | Size $l^*$ [cm] | QoS met? | #Iterations | OV $\sigma^*$ [dBsm] | Size $l^*$ [cm] |
| 1×2 | ✓ | 8 | 22.23 | 68.83 | ✗ | 5 | – | – | ✗ | 5 | – | – |
| 2×2 | ✓ | 9 | 22.12 | 68.09 | ✓ | 6 | 22.07 | 70.31 | ✓ | 9 | 22.07 | 50.27 |
| 2×3 | ✓ | 9 | 22.13 | 68.09 | ✓ | 7 | 22.12 | 67.34 | ✓ | 9 | 22.14 | 51.76 |
| 3×3 | ✓ | 7 | 22.05 | 67.34 | ✓ | 8 | 22.18 | 68.83 | ✓ | 8 | 22.10 | 53.98 |
| 3×4 | ✓ | 7 | 22.05 | 67.34 | ✓ | 8 | 22.16 | 68.83 | ✓ | 8 | 22.11 | 68.83 |
| 4×4 | ✓ | 7 | 22.09 | 67.34 | ✓ | 7 | 22.14 | 91.09 | ✓ | 8 | 22.16 | 71.80 |
| 4×5 | ✓ | 7 | 22.07 | 67.34 | ✗ | 5 | – | – | ✓ | 9 | 22.11 | 76.99 |
| 5×5 | ✓ | 7 | 22.05 | 67.34 | ✗ | 5 | – | – | ✓ | 8 | 22.10 | 77.73 |
| 5×6 | ✓ | 7 | 22.03 | 67.34 | ✗ | 5 | – | – | ✓ | 7 | 22.22 | 79.22 |
| 6×6 | ✓ | 7 | 22.00 | 67.34 | ✗ | 5 | – | – | ✓ | 5 | 22.23 | 88.13 |

– Smallest IRS $l^*$. – Max. common in-beam gain $\sigma^*$ with min. size $l^*$.
– Matches Fig. 7a: 2×2 HELIOS with $l$ = 50 cm in FR2 ⇒ $\sigma^*$ = 21.9 dBsm.

**TABLE 4.** **Cross-validation of design process: Change of communication requirements, e.g., *broader reflection* ($\Delta\phi_o = \Delta\theta_o$ = 10°) *with reduced in-beam gain* ($\sigma_{QoS}$ = 12 dBsm) compared to Tab. 3, leads to different IRSs.**

| | 3.7 GHz (FR1) | | | | 15.0 GHz (FR3) | | | | 27.1 GHz (FR2) | | | |
|---|---|---|---|---|---|---|---|---|---|---|---|---|
| M×N Modules | QoS met? | #Iterations | OV $\sigma^*$ [dBsm] | Size $l^*$ [cm] | QoS met? | #Iterations | OV $\sigma^*$ [dBsm] | Size $l^*$ [cm] | QoS met? | #Iterations | OV $\sigma^*$ [dBsm] | Size $l^*$ [cm] |
| 1×2 | ✗ | 5 | – | – | ✗ | 5 | – | – | ✗ | 5 | – | – |
| 2×2 | ✓ | 6 | 12.22 | 70.31 | ✓ | 6 | 12.02 | 46.56 | ✗ | 5 | – | – |
| 2×3 | ✓ | 6 | 12.21 | 70.31 | ✓ | 3 | 12.06 | 52.50 | ✗ | 5 | – | – |
| 3×3 | ✓ | 4 | 12.02 | 76.25 | ✓ | 8 | 12.13 | 62.89 | ✓ | 8 | 12.23 | 51.02 |
| 3×4 | ✓ | 4 | 12.10 | 76.25 | ✓ | 5 | 12.19 | 64.38 | ✓ | 20 | 12.05 | 53.81 |
| 4×4 | ✓ | 8 | 12.17 | 98.52 | ✓ | 7 | 12.17 | 73.28 | ✓ | 9 | 12.12 | 53.24 |
| 4×5 | ✗ | 5 | – | – | ✓ | 4 | 12.18 | 76.25 | ✓ | 12 | 12.14 | 62.43 |
| 5×5 | ✗ | 5 | – | – | ✓ | 9 | 12.17 | 87.38 | ✓ | 6 | 12.24 | 70.31 |
| 5×6 | ✗ | 5 | – | – | ✓ | 14 | 12.15 | 84.21 | ✓ | 7 | 12.23 | 85.16 |
| 6×6 | ✗ | 5 | – | – | ✓ | 5 | 12.23 | 88.13 | ✓ | 5 | 12.21 | 88.13 |

– Smallest IRS $l^*$. – Max. common in-beam gain $\sigma^*$ with min. size $l^*$.
– Matches Fig. 8a: 3×3 HELIOS with $l$ = 50 cm in FR2 ⇒ $\sigma^*$ = 11.8 dBsm.

Tab. 3 also provides insights into how IRSs have to be dimensioned for use in different spectra, such as for 3.7 GHz in FR1 and 15.0 GHz in FR3, when requiring the same performance metrics. For the 15.0 GHz case, it can be observed that module arrangements with 20 or more modules cannot attain $\sigma^* \geq \sigma_{QoS}$ given the upper size bound $l_{max}$ = 100 cm. This adheres to our prior results that the use of too many modules incurs a loss. Interestingly, the smallest HELIOS footprints are both 67.34 cm × 67.34 cm; however, the 15 GHz variant would leverage 2 × 3 modules, whereas the 3.7 GHz IRS could use 3 × 3 to 6 × 6 arrangements. Also, the 1 × 1 to 2 × 3 are just a bit larger. The reason for this is the inherently broader beamwidth at lower frequencies, cf. [54], so that the performance becomes nearly independent of the number of modules leveraged, given the small targeted beamwidth, which is very similar to what can be seen in Fig. 7a for $\Delta\phi_o, \Delta\theta_o \to 0°$. Given these options, the 16-module (4 × 4) option should be used as it attains the smallest size along with the highest headroom over $\sigma_{QoS}$. It is noted that other $M \times N$ constellations could also be selected, e.g., based on the least required IRS geometry volume to reduce costs. Overall, considering the RCS formula in (2), an increase in IRS panel size is what was to be expected considering the reduction of operating frequency, i.e., increase in wavelength $\lambda$.

The previous results are corroborated via Tab. 4, which presents the results of the full-blown design process being utilized to attain the smallest IRSs that guarantee a reduced $\sigma_{QoS}$ of 12 dBsm, however, over a much larger service area with a 10° horizontal and vertical beamwidth. For the carrier frequency of 27.1 GHz, the 3×3 HELIOS module arrangement results in the smallest side lengths of 51.02 cm, which is, as expected, just barely larger than the 50 cm 3 × 3 IRS in Fig. 8a that would result in an insufficient $\sigma^*$ of 11.8 dBsm. Hence, the size optimization process for multiple module arrangements again confirmed our findings from the previous case studies. For the 15.0 GHz operating frequency, Tab. 4 identifies a 2 × 2 IRS with 46.56 cm side lengths. This shows that even for lower frequencies, an IRS can be smaller than the one at higher frequencies, which stems from the RCS formula for conductive surfaces yielding different gains and beamwidths. Reducing the frequency further down to 3.7 GHz, the optimal HELIOS again features a 2 × 2 module array, however, with the highest overall width and height of 70.31 cm. Hence, Tab. 4 confirms the results in the context of Tab. 3: HELIOS geometries that are custom-tailored for lower carrier frequencies (i.e., FR1 spectrum) will require a larger mounting space than IRSs for FR2/FR3 frequencies to attain the same reflection characteristics in terms of horizontal and vertical beamwidths $\Delta\phi_o, \Delta\theta_o$, and minimum in-beam RCS $\sigma^*$.

## IV. MEASUREMENTS-BASED REFLECTOR EVALUATION

This section employs the proposed and validated IRSs design process from Sec. III to custom-tailor and manufacture four HELIOS IRSs in IV-A exhibiting distinct desirable far-field reflection behaviors. They are experimentally validated in two distinct measurement scenarios[2]: After introducing the methodology of the laboratory validation of the produced panels in Sec. IV-B, the results of these near-field measurements are provided and discussed in Sec. IV-C. The second measurement setup then sees the deployment of the IRS samples in an urban outdoor scenario with off-the-shelf cellular mmWave devices, as presented in Sec. IV-D. Sec. IV-E subsequently evaluates the acquired channel and link performance metrics.

### A. Custom Reflector Design for Experimentation

Based on our systematic performance study in Sec. III-B, this section leverages the proposed design process with *symmetry* conditions from Sec. III-A to customize and manufacture four HELIOS IRSs serving as the devices under test (DUTs) within the two measurement campaigns in Secs. IV-B to IV-E.

**IRS Design Goals:** The operating frequency of 27.3 GHz was selected as it falls within the FR2 (mmWave) band and is the mid-frequency of the real mmWave network used in the field study. Communication at such high frequencies is characterized by higher path loss and limited coverage compared to FR1 (sub-6 GHz) spectrum. This makes it a compelling scenario for evaluating the performance of IRSs, whose primary role is to enhance coverage and compensate for such propagation challenges. The chosen angles of incidence and departure reflect practical deployment constraints and common urban use cases, where signals typically impinge on the IRS at moderate angles due to UE and BS placements ($|\phi|, |\theta| \leq 45°$) [84], [85]. These angles allow for a realistic assessment of IRS behavior in NLOS conditions. However, due to operational limitations of laboratory equipment and otherwise resulting high methodical complexity for larger field measurement scenarios, the experimental work is limited to the horizontal plane such that the elevation angle of incidence $\theta_{in}$, the center elevation reflection angle $\theta_{o,c}$, and measured elevation reflection angles $\theta_{out}$ are all set to 0°. Nonetheless, a $\Delta\theta_o = 3°$ vertical beamwidth is enforced to challenge the design process.

Considering the previous fixation of elevation space characteristics, the four IRSs ought to exhibit diverse characteristics in the horizontal plane in order to highlight the custom-tailored HELIOS IRSs' capability to redirect the incident EM wave into different directions with different beamwidths. The azimuth angle of incidence $\phi_{in}$ is common with −45°. IRSs {#1, #2} reflect to center azimuth reflection angle $\phi_{o,c} = 0°$, whereas IRSs {#3, #4} to $\phi_{o,c} = 30°$. Additionally, IRSs {#1, #3} shall exhibit a horizontal reflection beamwidth of $\Delta\phi_o = 3°$ (like the vertical beamwidth), whereas IRSs {#2, #4} aim for a horizontally broader reflection with $\Delta\phi_o = 10°$. The angular resolution for the respective reflection beam spaces $\Omega_{out}$, based on the parameter set $\{\phi_{o,c}, \theta_{o,c}, \Delta\phi_o, \Delta\theta_o\}$ (cf. (9)), is fixed to 0.1° like in the systematic performance assessment of the custom design process in Sec. III-B.

Overall, all the reflector panels shall have the size of 29.7 cm × 29.7 cm to not exceed the quiet zone of the anechoic chamber, which is employed for the laboratory experiments (see the respective methodology section in Sec. IV-B). Hence, the reflector size optimization does not need to be employed. Thus, there is target RCS value $\sigma_{QoS}$. The predetermined panel size is nonetheless much larger than ten wavelengths, such that we can characterize the four panels as large-scale IRSs which are large enough for the deployment in future 6G mmWave networks [10], for example, to improve coverage in NLOS situations in urban canyons, see the respective methodology section for the field trial in Sec. IV-D. Considering that the panel size was predetermined, the module arrangement is set according to the beamwidth (cf. results in Sec. III-B), i.e., 2 × 2 for the narrow beams of HELIOS #1 and #3, and 4 × 4 for reflectors #2 and #4. Tab. 5 summarizes the above-presented details according to incident EM wave parameters $\Omega_{in}$, reflection beam configuration $\Omega_{out}$, and HELIOS geometry aspects $\mathcal{H}$.

**Synthesis and Production of Four HELIOS IRSs:** The design process was conducted for the previously presented requirements using `MATLAB` running on a single CPU core

**TABLE 5. System setup-dependent design constraints for lab and field measurement campaigns with HELIOS IRSs #1 – #4.**

| | Parameters (cf. Fig. 2) | Description/Value |
|---|---|---|
| $\Omega_{in}$ | Carrier frequency | $f = 27.3$ GHz |
| | Azimuth angle of incidence | $\phi_{in} = -45°$ |
| | Elevation angle of incidence | $\theta_{in} = 0°$ |
| $\Omega_{out}$ | Center azimuth reflection angles | $\phi_{o,c} = 0°$ (#1, #2) *or* 30° (#3, #4) |
| | Horizontal beamwidth | $\Delta\phi_o = 3°$ (#1, #3) *or* 10° (#2, #4) |
| | Center elevation reflection angle | $\theta_{o,c} = 0°$ |
| | Vertical beamwidth | $\Delta\theta_o = 3°$ |
| | Angular resolution | $\Delta\phi_{o,res} = \Delta\theta_{o,res} = 0.1°$ |
| $\mathcal{H}$ | Reflector side lengths | $N \cdot a = M \cdot b = 29.7$ cm |
| | IRS module arrangement | $M = N = 2$ (#1, #3) *or* 4 (#2, #4) |
| | Module footprint | $a = b = 13.51\lambda$ *or* $6.76\lambda$ |
| | Module tilt angles | $\{\alpha_{1,1}, \ldots, \alpha_{M,N}, \beta_{1,1}, \ldots, \beta_{M,N}\}$ via *symmetry*-based beam shaping (Sec. III) |

$\Omega_{in}$: Incident wave. $\Omega_{out}$: Reflection beam. $\mathcal{H}$: HELIOS geometry.

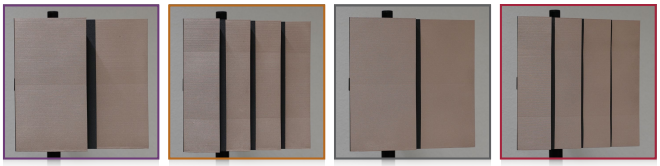

(a) HELIOS #1 (b) HELIOS #2 (c) HELIOS #3 (d) HELIOS #4

**FIGURE 10. Four custom-tailored HELIOS IRSs serve as DUTs for beyond-LOS mmWave communications, depicted in pole mounting.**

[2] Selected aspects of the laboratory measurements in Secs. IV-B to IV-C appear in the conference paper [71], and selected aspects of the field measurements in Secs. IV-D to IV-E in the submitted conference paper [73]. Both papers provide a broad comparison of available IRS prototypes, whereas this article provides an in-depth experimental investigation of the HELIOS reflectors.

with a 3.5 GHz clock rate. The GA required between 5,223 and 28,320 trial geometries per IRS, thus resulting in customization times[3] of 16.26 s for IRS #1, 157.98 s for IRS #2, 14.57 s for IRS #3, and 98.98 s for IRS #4. Therefore, customization of the reflecting geometries with broad reflection beams utilizing more modules was computationally more complex. The identified geometries were then 3D-printed using PLA material and subsequently spray-coated with conductive varnish [20][4]. It is noted that self-shadowed patches of the surface were identified by the reflection model and specifically not coated, such that the match between real reflection behavior and the analytical model being used for the customization remains high [54]. The resulting HELIOS reflectors are presented in Fig. 10, showcasing unique tilt angle distributions.

**Preliminary Assessment of Custom HELIOS Samples:** Before the experiments in the subsequent sections, we conduct a preliminary study of the FF reflection behavior of the analytical model-based IRS configurations by comparing them to the RCS reflection patterns attained by EM simulations with `Ansys HFSS` [82], as depicted in Fig. 11. It can be observed that IRSs {#1, #2} reflect toward the center azimuth angle $\phi_{o,c} = 0°$, whereas {#3, #4} toward $\phi_{o,c} = 30°$. Similarly, it can be seen that IRSs {#2, #4} exhibit a horizontally broadened reflection beamwidth of 10°, whereas IRSs {#1, #3} have a more narrow horizontal beamwidth $\Delta\phi_o$ of just 3°. This is both as desired. Particularly for HELIOS IRSs {#2, #4} with broad horizontal reflections, it can be observed that the reflection gain is maximal in the horizontal plane, i.e., there is a falloff of up to about 10 dB in in-beam RCS if the UE is at elevation angles $\theta_{out} \neq 0°$. For example, reflector #4 exhibits at least 10.2 dBsm in the desired reflection beam space, which corresponds to the maximized OV $\sigma^*$ of our proposed design process. However, the peak in-beam gain is 18.3 dBsm such that UEs may be overprovisioned opportunistically by up to 8.1 dB over the guaranteed reflection gain $\sigma^*$. This fits into the in-beam gain range studied in the context of Fig. 7d. Similarly, HELIOS #1 attains $\sigma^* = 12.1$ dBsm, whereas IRS #2 realizes 10.5 dBsm, and IRS #3 attains the maximum guaranteed in-beam gain of 12.8 dBsm. From this, it can be extracted that the broader reflection beams of IRSs {#2, #4} result in an OV reduction of up to 2.6 dB, which aligns well with the beamwidth sensitivity analysis in Sec. III-B.

The match between the analytic prediction of the reflection pattern, which was used by our design process, and the previously discussed EM simulation results, cf. Fig. 11, is assessed briefly to validate that their behaviors align. For brevity, this is done considering only the horizontal reflection pattern slices ($\theta_{out} = 0°$) shown in Fig. 12. Like in our previous work [54], a high match can be observed in the target beam areas being utilized in the scope of the design process, whereas deviations get stronger with increasing deviation between $\phi_{out}$ and beam center angle $\phi_{o,c}$. However, because RCS values outside of the target beam area, for which the mismatch can be high in some cases, are not utilized by our design process, this deficiency of the PO-based reflection model has no negative effect [54]. Hence, the four HELIOS geometries, which were quickly designed using the analytical model, agree with the complex EM simulations particularly well in the important main lobe region, indicating similar behavior in later FF deployments (cf. Secs. IV-D to IV-E).

[3] With parallelization, optimization times well under 10 s per IRS are attained.
[4] Further details regarding the sustainability of this approach, with respect to cost and lifespan, are given in the Appendix.

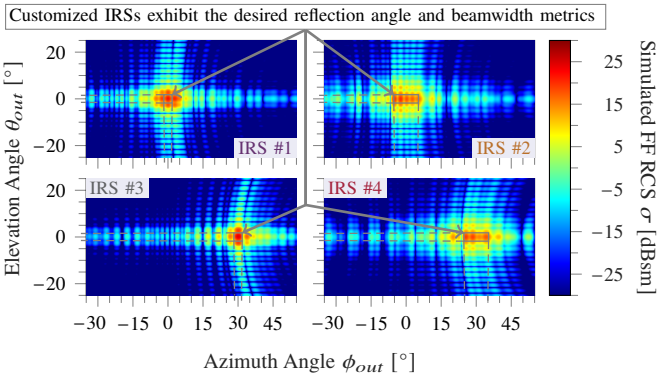


**FIGURE 11.** **Far-field reflection patterns of synthesized HELIOS IRSs exhibit high gains in the respective target reflection regions.**

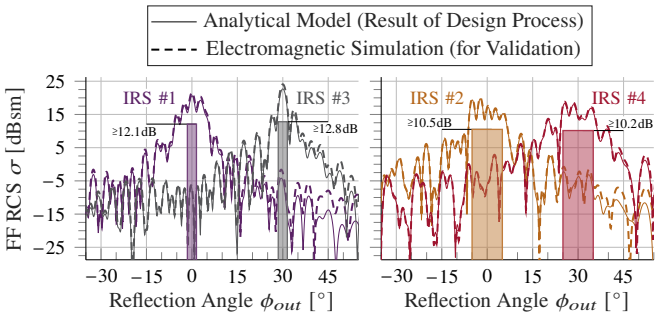


(a) Narrow beam: $\Delta\phi_o = 3°$ (b) Broadened beam: $\Delta\phi_o = 10°$

**FIGURE 12.** **Horizontal FF reflection of the IRSs under test. Gains in target area are up to about 10 dB above the maximized minimum value (OV).**

### B. Methodology of Laboratory Near-field Measurements

The measurements are conducted in a modified multi-probe CATR anechoic chamber [86], ensuring a controlled radio environment with suppressed multipath effects, as shown in Fig. 13. A CATR reflector with rolled edges is employed together with a transmitter (TX) feed horn antenna to attain a laser-aligned intermediate far-field illumination of the IRS. The quiet zone has a length of 30 cm, which is larger than the IRSs under test. An NF receiver (RX) probe is used to measure the bistatic FF to NF reflection pattern with a radius of about 0.5 m. It is mounted on a computer-controlled rotating platform for systematic measurement of reflection patterns at different angles $\phi_{out}$ with an angular resolution of 0.5°. It is noted that both antennas are dual-polarized with coaxial outlets for horizontal and vertical polarization. In the following paragraphs, it is described how the setup is used to acquire various performance metrics, as summarized in Tab. 6.

A four-port vector network analyzer (VNA) [87] is em-

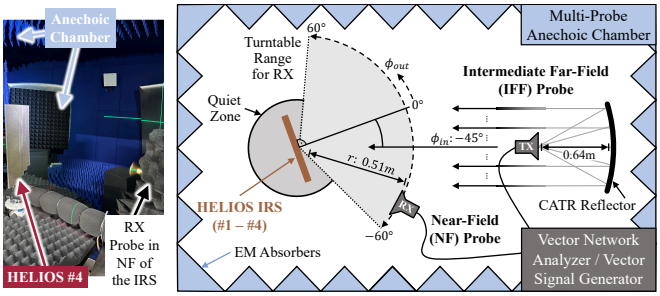


(a) IRS under test. (b) Top-view sketch of laboratory setup.

**FIGURE 13. Overview of near-field measurements of HELIOS IRS samples.**

**TABLE 6. Laboratory measurement setup details.**

| | Parameter | Description/Value |
|---|---|---|
| Overview | Transmit Power | $P_{TX} = -14.4$ dBm |
| | Antenna Gains | $G_{TX} = 9.5$ dBi, $G_{RX} = 15.1$ dBi |
| | Incidence Angle at IRS | $\phi_{in} = -45°$, $\theta_{in} = 0°$ |
| | Incident Wave at IRS | Intermediate Far-Field (FF) using CATR Reflector |
| | Reflected Wave at RX | Near-field (NF) of IRS, i.e., 0.51 m to IRS origin |
| | Measured IRSs | HELIOS #1 – #4, cf. Sec. IV-A |
| Power Meas. | Multipath Suppression | Time-gated Measurements |
| | Measured Angles | $\phi_{out} \in [-60° : 0.5° : 60°]$, $\theta_{out} = 0°$ |
| | Measured Frequencies | 24 GHz to 42 GHz with 10 MHz Resolution |
| | Measured Polarization | Horizontal (H-pol.) and Vertical (V-pol.) |
| | Performance Metrics | Path Gain, Specular Suppression Ratio (SSR) |
| Quality Meas. | Carrier Frequency | $f = 27.0$ GHz, i.e., $\lambda = 1.1$ cm |
| | Signal Bandwidth | $B = 700$ MHz |
| | Measured Modulations | {128, 256, 1,024} QAM |
| | Measured Angles | $\phi_{out} = \phi_{o,c} = \{0°, 30°\}$, $\theta_{out} = \theta_{o,c} = 0°$ |
| | Measured Frequencies | 26 GHz to 28 GHz with 2 MHz Resolution |
| | Measured Polarizations | Vertical (V-pol.) |
| | Performance Metrics | In-band: Error Vector Magnitude (EVM), Path Gain. Out-of-band: Adjacent Channel Power Ratio (ACPR) |

ployed to measure the angular reflected power profile along both polarizations simultaneously. The measurements are conducted for the 24 GHz to 42 GHz spectrum with a 10 MHz resolution. Moreover, time gating with a 38.0 ns to 41.5 ns window, which accounts for the chamber dimensions and IRS-based propagation path, is applied to additionally mitigate undesired system effects such as multipath reflections. The main performance metric of these measurements is the path gain (i.e., inverse of path loss), which relates the measured received power level to the transmit power level. As it is available over an 120° angular range, the overall NF reflection behavior of the IRS can be assessed including main- and sidelobes. Furthermore, the specular suppression ratio (SSR) metric is extracted from this data by comparing the power at the natural reflection angle ($\phi_{out} = 45°$) to that in the IRS reflection beam. These two metrics, path gain and SSR, are essential for understanding how effectively the IRS redirects energy and suppresses unwanted specular components, thus reflecting its ability to control wavefronts to improve coverage. Both are subsequently analyzed in Sec. IV-C to measure the beamforming performance and energy steering accuracy of each IRS prototype.

It is noted that this article also compared the measurement data against NF simulations with `Ansys HFSS` [82] in terms of the Poynting vector power flux metric. Furthermore, this is complemented by FF behavior (bistatic RCS metric) predicted by EM simulations and the analytical model, cf. Sec. IV-A. The combination of simulation and measurement allows for validation of both the designed IRS behavior and the predictive accuracy of modern modeling tools, which further contextualizes the results discussed in Sec. IV-C.

Besides the above power measurements, the impact of the four IRSs on the channel quality in the reflection beam is studied. The RX probe is therefore positioned at the reflection angle with the peak received power level. Against this background, these measurements additionally leverage a vector signal analyzer (VSG) [88] to generate a 700 MHz broad and 128- to 1,024-quadrature amplitude modulation (QAM) modulated mmWave signal along the vertically polarized channel. The in-band performance metrics of these measurements are error vector magnitude (EVM) and path gain. EVM offers a clear indication of signal quality decline caused by IRS-induced distortion, which is especially important at higher-order modulation schemes used in FR2. Path gain in this context helps relate it to the passive beamforming gain under real-world signal conditions. Moreover, out-of-band impact on upper and lower neighboring bands contained in the 26 GHz to 28 GHz range is assessed with the adjacent channel power ratio (ACPR) metric. ACPR evaluates any spectral regrowth or leakage caused by the IRS, which is crucial for meeting spectral mask regulations and ensuring coexistence with nearby channels. These quality-related metrics are examined in Sec. IV-C to assess the IRSs' suitability for spectrally efficient, high-throughput communications.

### C. Results and Discussion of Lab Measurements

**NF Path Gain Characteristics:** We start by analyzing the measured path gain heatmaps over frequency and reflection angle for HELIOSs #1 and #3, shown at the top and bottom of Fig. 14, respectively. These measurements outline differences in reflection behavior. Specifically, HELIOS IRS #1 directs the reflected energy predominantly toward angles near the broadside direction ($\theta_{out} = 0°$), whereas HELIOS IRS #3 reflects toward a more oblique angle ($\theta_{out} = 30°$). Hence, these observations align well with the target angles specified during the design phase, cf. Sec. IV-A. It is noted that a similar behavior would be observed for IRSs {#2, #4} (not depicted for brevity), with the former reflecting toward the same direction as IRS #1, whereas the latter into the same center reflection direction as IRS #3.

A comparison between vertical and horizontal polarization, shown on the left and right sides of Fig. 14, indicates strong similarities in the reflection behavior. It is again noted that the same behavior can also be observed for IRSs {#2, #4}, but it is not depicted for brevity. Overall, this confirms that the HELIOS reflectors effectively support both polarizations. The observed behavior highlights the potential for polarization-separated multiple-input multiple-output (MIMO) operation,

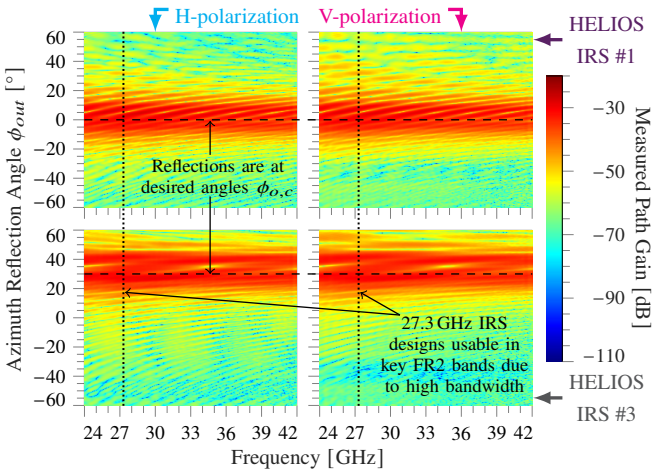


**FIGURE 14.** **Measured NF path gains over frequency and reflection angle of reflectors *(top row)* #1 and *(bottom row)* #3. Regardless of *(left)* vertical and *(right)* horizontal polarization, the incident wave is successfully reflected toward the respective target angles, such that two MIMO layers are supported. The obtained data further underline a desirable support of the entirely passive IRSs for a multi-GHz wide range of FR2 spectrum.**

allowing dual-stream transmission within the same spatial footprint, which is a key capability for high-throughout and -capacity mmWave communication systems.

Additionally, the reflection beams in Fig. 14 persist consistently across the entire measured frequency range, spanning from 24 GHz to 42 GHz. The reason for this behavior mainly stems from the 3D macro-geometry of the reflectors, i.e., natural reflection with large flat surfaces, which stands in contrast to the wave synthesis of synthetic IRSs. This wideband performance is particularly relevant as it encompasses the major FR2 mmWave bands used globally, such as the 28 GHz n257 band in Europe and the 38 GHz n260 band in the United States. These empirical results further support earlier simulation-based studies, including [42], which predicted HELIOS reflection characteristics across an even wider span from 0.5 GHz to 100 GHz. However, while the results show that our IRSs designed for 27.3 GHz work reasonably well across other frequencies, the data in Fig. 14 also reveal frequency-dependent fades in the reflected beam. These dips can cause degraded link quality at certain frequencies and emphasize the importance of customizing the IRS design to the target operational frequency band for the best performance of the wideband communication system. We further note that the IRS design process presented in Sec. III-A could be easily modified to consistently procure a broadband QoS-compliant minimum in-beam reflection gain, e.g., by optimizing jointly for the center as well as the edges of the targeted spectral communication band. Nonetheless, it is noted that the observed wideband characteristic may be undesirable in dense deployment scenarios with multiple mobile network operators operating in adjacent mmWave bands.

Fig. 15 offers a detailed comparison between measured and simulated reflection patterns for HELIOS #1 through #4 at the 27.3 GHz design frequency. The left column of all four subfigures shows vertical slices from the heatmaps contained in Fig. 14, illustrating NF path gain measurements for both horizontal and vertical polarizations. The right column displays the corresponding simulated power flux distributions (Poynting vector magnitude) predicted by EM simulations.

Starting with IRSs #1 and #3 (cf. Figs. 15a and 15c), it can be seen that UEs near the IRS benefit from wider reflection beams, while the reflection's angular spread narrows in the FF, as discussed in Sec. IV-A. This aligns with NF propagation behavior reported in literature, where proximity results in increased spatial coverage due to near-field diffraction effects. In contrast, the results for HELIOS {#2, #4} in Figs. 15b and 15d differ from this trend. While the reflection gets broader, it also moves outside the desired region. Accordingly, the gain in the desired reflection direction drops by at least 5 dB compared to IRSs {#1, #3}. Additionally, a fade in measured NF path gain can be observed at some of the angles for which HELIOS reflectors {#2, #4} attain high gains in the FF. Owing to this, IRS #2 incurs a 12.8 dB lower minimum in-beam gain than IRS #1. Similarly, IRS #4 has an 11.3 dB loss in OV

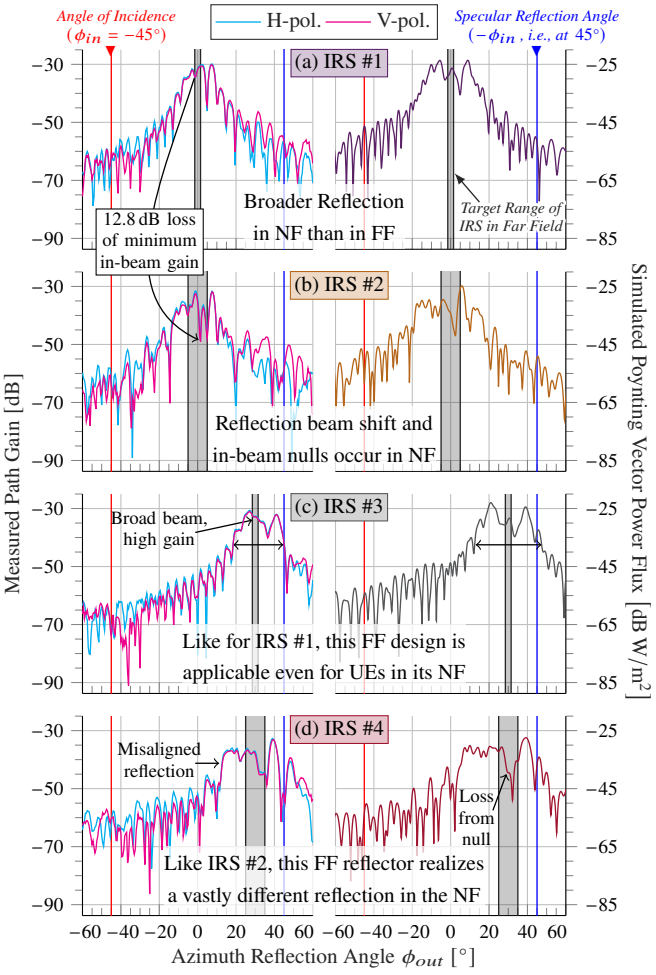


**FIGURE 15.** **Comparison between near-field *(left column)* path gain measurements and *(right column)* Poynting vector power flux simulations of HELIOS *(a)* #1, *(b)* #2, *(c)* #3, and *(d)* #4. Good match between NF measurements and NF simulations again confirms the proposed analytic FF HELIOS design process which was shown to match with FF simulations.**

against IRS #3 in the NF, whereas the difference in the FF would be smaller (≤ 2.6 dB, cf. Sec. IV-A). Overall, this shows that the FF IRS designs can perform well in the NF; however, this depends strongly on the IRS's configuration as well as the UE distance and angle from the IRS. We note that an improved NF reflection behavior can be achieved by using the proposed IRS customization process from Sec. III-A in conjunction with a distance-agnostic reflection model, as shown in [89]. Thus, with slight modifications of the implemented reflection beam shaping process, HELIOS IRSs could in future not just be optimized over a set of azimuth and elevation angles as in this work, but also for a set of distances.

Despite some specific deviations, the overall comparison between measurements and EM simulations shows a high level of consistency, with the highest match observable in Fig. 15d. The measured path gain profiles generally match the predicted power flux patterns, considering plausible sources of error such as slight IRS mounting misalignments, variations in receiver angle or position, and the exclusion of antenna pattern effects in the simulations. Importantly, this alignment substantiates the HELIOS design approach introduced in Sec. III: The close match between NF measurements and simulations confirms the reliability of the simulated and analytical FF behavior discussed in Sec. IV-A. Moreover, as assessed in Sec. IV-A and studied in-depth within [54], this simulated FF behavior aligns well with the analytical models used during the proposed design process of the considered HELIOS prototypes. Taken together, these results confirm the integrity of the entire design process, from theory and simulation to real-world deployment.

**NF Signal Integrity Characteristics:** Tab. 7 shows the performance of all four IRS samples for three different modulation and coding schemes (MCSs), i.e., 128-QAM at the top, 256-QAM in the middle, and 1,024-QAM at the bottom. The table reports four key performance metrics: The first one is the in-band path gain, which have already been discussed previously in the context of Figs. 14 and 15. With changes of less than 0.1 dB between the three modulation schemes, these performance values are independent of the MCS and therefore not discussed subsequently. Thus, we focus on the remaining three performance metrics from the laboratory measurement campaign: in-band EVM as well as low- and high-band ACPRs. It is noted that low EVM and ACPR values are desirable, as they reflect higher received signal quality – enabling high-performance, energy-efficient communications – and reduced signal leakage into adjacent channels, thereby minimizing interference with other transmissions. Moreover, over-the-air signal degradation can be assessed by a comparison of the transmit signal quality listed in the respective table column.

The 128-QAM transmit signal-based performance is considered at first: For IRS #1, it can be observe an in-band EVM of −46.7 dB, which is just 2.2 dB higher than on the TX side, thus underlining excellent in-band signal forwarding characteristics. Moreover, its performance is much better than for the other reflectors, particularly when compared to IRS #4 which has a 13.6 dB higher EVM with a value of −33.1 dB, indicating an approximately 20-times stronger signal distortion. In terms of spectral purity, IRS #1 also exhibits the lowest ACPRs in both low-band (−56.5 dB) and high-band (−48.1 dB) neighboring spectrum. Again, IRS #4 performs the worst here with ACPRs of −41.1 dB and −33.2 dB, respectively. This constitutes a 14.9 dB to 15.4 dB performance gap in the NF for the different custom FF reflection patterns of the HELIOS panels. It is particularly interesting to note that these quality metrics clearly correlate with the attained NF in-band path gains of the reflectors.

The same trend appears with the 256-QAM signal: IRS #1 again has the best EVM with −44.0 dB, but is closely followed by IRS #3 with 0.1 dB additional signal degradation. IRS #2 loses 5.4 dB and IRS #4 loses 10.7 dB against IRS #1. However, the gap is smaller than before. In regard to ACPR, IRS #1 is still performing best with −55.2 dB (low-band) and −48.5 dB (high-band). Here, it is interesting to note that all four HELIOS IRSs perform between 0.6 dB and 1.4 dB worse in the lower neighboring band than for the 128-QAM case, whereas 0.0 dB to 0.4 dB better in the upper neighboring band.

For the EVM value of the 1,024-QAM measurements, IRS #1 restores its EVM value of −44.0 dB, which it also exhibited for 128-QAM but missed by 2.6 dB in the 256-QAM case; in part because the transmit signal EVM is better in this case. The other three reflectors remain in their already established EVM performance brackets with a maximum delta of 0.5 dB over the three considered modulation schemes. Overall, it can therefore summarize that the EVM is weakly affected by the selected modulation scheme.

In regards of the ACPR values of the 1,024-QAM measurements, IRS #1 continues to be the best reflector with an over-the-air ACPR degradation of down to 9.3 dB, indicating that the HELIOS IRSs indeed effect the signal strength in the adjacent bands in relation to the signal band, which is as expected considering the multi-GHz bandwidth discussed in context of Fig. 14. Again, the upper-band ACPR degradation from the reflector is typically higher than the lower-band ACPR, which

**TABLE 7. IRS performance exhibits low dependence on utilized MCS.**

| | Performance Metric | Transmit Signal | Received Signal via HELIOS Reflector | | | |
|---|---|---|---|---|---|---|
| | | | IRS #1 | IRS #2 | IRS #3 | IRS #4 |
| 128-QAM | In-band Path Gain [dB] | 0.0 | −30.2 | −38.6 | −33.8 | −45.2 |
| | In-band EVM [dB] | −48.9 | −46.7 | −38.9 | −44.4 | −33.1 |
| | Low-band ACPR [dB] | −69.8 | −56.5 | −47.6 | −52.6 | −41.1 |
| | High-band ACPR [dB] | −70.2 | −48.1 | −39.9 | −44.8 | −33.2 |
| 256-QAM | In-band Path Gain [dB] | 0.0 | −30.1 | −38.7 | −33.8 | −45.1 |
| | In-band EVM [dB] | −51.1 | −44.0 | −38.6 | −43.9 | −33.3 |
| | Low-band ACPR [dB] | −65.4 | −55.2 | −46.8 | −51.2 | −40.5 |
| | High-band ACPR [dB] | −66.6 | −48.5 | −40.0 | −44.8 | −33.4 |
| 1,024-QAM | In-band Path Gain [dB] | 0.0 | −30.1 | −38.7 | −33.8 | −45.2 |
| | In-band EVM [dB] | −50.5 | −46.7 | −38.5 | −44.0 | −33.2 |
| | Low-band ACPR [dB] | −64.2 | −54.9 | −41.9 | −52.0 | −40.4 |
| | High-band ACPR [dB] | −65.9 | −48.4 | −39.9 | −44.5 | −33.2 |

Path Gain: High is good. EVM, ACPR: Low is good.

could be owing to increased reflection directivity at higher frequencies [54]. Overall, Tab. 7 yields that the ACPRs in the upper and lower bands are only weakly dependent on the MCS.

Summarizing the results from Tab. 7, the EVM and ACPR metrics are only weakly dependent on the employed MCS, just like the path gain metric. Instead, a strong impact of the employed HELIOS IRS panel was observed along with a strong correlation between attained signal strength (i.e., path gain) and observed signal quality (i.e., EVM and ACPR). It is now put in the context of the observations in Sec. III that the geometry-based HELIOS IRSs with few modules may realize high reflection gains in a small angular area (cf. IRSs #1 and #3 with $2\times2$ module arrangement), whereas IRSs with numerous modules are better suited for broad reflection with a weaker guaranteed reflection gain in that angular region (cf. IRSs #2 and #4 using $4\times4$ modules). Correspondingly, the path gain (and thus, received signal strength) observed at the RX position depends strongly on the RCS of the IRS. If it is low, e.g., for the broad reflecting IRSs #2 and #4, the signal quality along the artificial reflection path drops accordingly.

The attained in-band signal integrity of the reflectors from this work are briefly compared with other static and reconfigurable IRSs in exactly the same measurement setup, cf. [71, Tab. 3]. It is noted that IRSs $\{\#1, \#2\}$ from this work are denoted as static reflectors $\{D,\ E\}$ in [71]. The following for the delta between EVM of the transmit signal and the received signal are found: Across the three modulations, IRS #1 (*Ref. D*) results in a mean EVM degradation of 0.20 %, whereas IRS #2 (*Ref. E*) yields 0.65 %. The other three static reflectors were found to exhibit 0.33 % to 0.45 % over-the-air EVM degradation. Hence, this places IRS #1 as the best of all five static reflectors, whereas IRS #2 is the last. The latter result is intuitive considering that this article previously found the panel to be unsuitable for NF communications in Fig. 15. Nonetheless, all the static reflectors perform much better than the reconfigurable reflectors[5], which exhibited EVM degradation of 2.71 % to 5.75 %, i.e., up to 29-times worse signal integrity behavior than the best-performing HELIOS IRSs.

[5]This statement is also supported by recent external measurements, e.g., for a commercial semi-passive reconfigurable IRS, which realized −16.6 dB received signal EVM at best [72]. The attained signal integrity is thus 16.5 dB to 30.1 dB worse than the best and worst received signal EVMs of the four static-passive IRSs in Tab. 7.

**TABLE 8. Power in the customized IRS reflection beam dominates the specular component (SSR ≫ 0 dB), indicating efficient incident power redirection capabilities for beyond-LOS communications as well as reflection suppression capabilities for interference mitigation.**

| | **Max. SSR [dB]** based on five metrics: | **HELIOS #1** $\phi_{out}\in[-1.5, 1.5]°$ | **HELIOS #2** $\phi_{out}\in[-5, 5]°$ | **HELIOS #3** $\phi_{out}\in[28.5, 31.5]°$ | **HELIOS #4** $\phi_{out}\in[25, 35]°$ |
|---|---|---|---|---|---|
| NF | Path Gain H-pol. *(M)* | 26.3 | 27.1 | 9.1 | 19.5 |
| NF | Path Gain V-pol. *(M)* | 25.9 | 26.2 | 9.6 | 16.0 |
| NF | Power Flux *(S)* | 25.8 | 23.7 | 5.0 | 6.1 |
| FF | RCS *(S)* | 29.5 | 29.4 | 24.3 | 17.0 |
| FF | RCS *(A)* | 34.4 | 33.3 | 26.0 | 18.0 |

FF: Far Field. NF: Near Field. *(M)* Measurement. *(S)* EM Simulation. *(A)* Analytical Model.

The comparison of IRSs #1 and #2 with other static and reconfigurable IRSs from [71] is continued for the low- and high-band ACPR metrics. On average over the three MCSs, the static reflectors attain low-band ACPRs between −55.35 dB and −45.40 dB, whereas the reconfigurable reflectors attain between −32.04 dB and −26.34 dB. This shows that static reflectors have less impact on the lower neighboring band than the reconfigurable reflectors. Similarly, the static reflectors attain better high-band ACPRs between −48.34 dB and −39.92 dB, whereas the reconfigurable reflectors attain between −31.29 dB and −25.36 dB. This confirms that the static reflectors also have less impact on the upper neighboring band than the reconfigurable reflectors. Importantly, IRS #1 (*Ref. D*) with −55.35 dB and −48.34 dB lower- and upper-band ACPRs has the least impact on the neighboring bands, thus pointing out that the HELIOS IRSs can offer the least signal leakage than other reflector architectures.

**Specular Reflection Suppression Characteristics from NF to FF:** Tab. 8 presents a comparative analysis of the power redirection capabilities of four HELIOS IRSs, emphasizing the ability to suppress power in the specular reflection direction ($\phi_{out} = -\phi_{in} = -45.0°$) while concentrating energy in a customized beam direction. The effectiveness of each IRS configuration is characterized by the previously defined maximum SSR, which indicates how effectively the reflector can redirect energy away from the undesired specular path into the intended angular reflection direction. The SSR metric is determined for NF and FF regimes based on different underlying data, such as the measured NF path gains for horizontal and vertical polarizations, the simulated NF Poynting vector power flux density, as well as the simulated and modeled FF RCS values.

Among the four reflectors, HELIOS #1 and #2 exhibit the strongest suppression of specular reflection, with beam redirection tightly focused within angular ranges of $\phi_{out} \in [-1.5°, 1.5°]$ and $\phi_{out} \in [-5.0°, 5.0°]$, respectively. In the NF region, HELIOS #2 achieves the highest SSRs in terms of measured path gains of the horizontal (27.1 dB) and vertical (26.2 dB) polarizations. Thus, HELIOS #2 slightly outperforms HELIOS #1 by up to 0.8 dB. However, IRS #1 attains a better match between the measurements-based SSR values and the simulative power flux-based SSR value. Moving on to the prognosed FF SSR based on the RCS reflection patterns of IRSs $\{\#1, \#2\}$, even better suppression of the specular reflection with an SSR of up to about 34 dB should be expected in large-scale deployments.

In contrast, HELIOS #3 and #4 exhibit significantly poorer SSR performance across all five metrics, but particularly for the NF measurements, where HELIOS #3 attains only 9.1 dB (H-pol) and 9.6 dB (V-pol) SSR, whereas HELIOS #4 fares better with SSR values of 19.5 dB (H-pol) and 16.0 dB (V-pol). The reason for this is a combination of two aspects: First, considering our recent reflection modeling activities in [54], this can be attributed to the small angular offset between intended center reflection angle range ($\phi_{o,c}$) and specular reflection angle ($-\phi_{in}$), which is now only 15° compared

to 45° for IRSs {#1, #2}. For this reason, natural reflection sidelobes falling into the specular direction may still have high power. For the NF SSR, a second deteriorating factor needs to be considered, which we have already discussed in the prior comparison of the angular NF reflection profiles in Fig. 15 and the custom-designed FF behavior in Sec. IV-A: Reflections in the NF are even broader such that stronger reflections can be observed at the specular direction. Against this background, it can also be explained well why IRS #3 in Tab. 8 exhibits a better RCS pattern-based SSR in the FF region: First, there is no NF-based reflection broadening in the FF. Second, the energy is reflected rather to the azimuth angle range $\phi_{out} \in [28.5°, 31.5°]$ instead of $\phi_{out} \in [25.0°, 35.0°]$, such that there is an additional 3.5° reflection beam separation to the specular reflection direction ($-\phi_{in} = 45°$).

When comparing the attained SSR metric of the HELIOS reflectors #1 and #2 from this work (cf. Tab. 8) with other static and reconfigurable IRSs in exactly the same measurement setup, cf. [71, Tab. 2], one finds the following: Conventional IRS designs (static and reconfigurable) achieve relatively low SSRs ranging from −4.5 dB to 15.3 dB, with the reconfigurable IRSs attaining no more than 8.4 dB. This is corroborated by recent external measurements of a commercial semi-passive reconfigurable IRS, which attained up to about 10 dB SSR in the best case [72]. In contrast, the geometry-based approach HELIOS attains about 27 dB in the NF with slight variations depending on the IRS under test and the polarization. The reason for this behavior mainly stems from the 3D macro-geometry of the reflectors compared to conducting wave synthesis like typical IRSs. Nonetheless, with a superior SSR performance with a delta of 12 dB to 31 dB, our approach is more suitable to negate natural specular reflection, thus outlining that a deployment of HELIOS IRSs would also be highly suitable for deliberate energy redirection-based suppression of interfering propagation paths, e.g., from other BSs operating in the same frequency band.

### D. Methodology of Urban Field Trial

To assess the performance and practical effectiveness of the passive HELIOS reflectors in real-world urban settings, we conducted an extensive far-field test in the Plaza de la Constitución in Málaga, Spain. This pilot site was intentionally selected for its dense city layout, which creates challenging NLOS conditions typical of mmWave communication environments expected in future 6G deployments [90]. The test scenario, shown in Fig. 16, illustrates these propagation conditions where direct paths are blocked by buildings, requiring alternative methods for delivering high-throughput connectivity. The experimental setup included a commercially available standalone (SA) mmWave BS operating in the FR2 spectrum and a commercial-of-the-shelf (COTS) mmWave-capable UE. The hardware configurations, antenna array details, and system settings are outlined in Tab. 9, as described below.

The BS was positioned about 10 m from the intended IRS

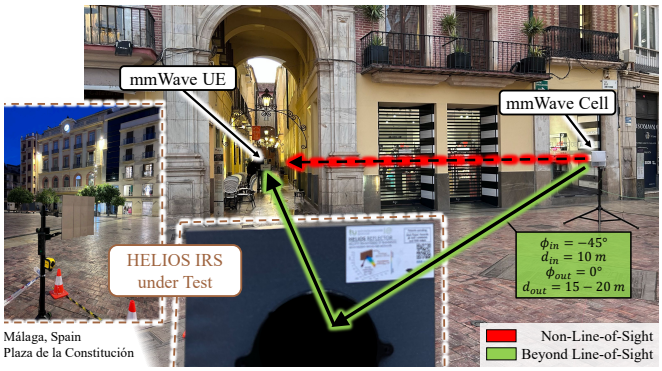


**FIGURE 16. Overview of outdoor measurements with cellular mmWave system utilizing HELIOS IRSs for improved connectivity in street canyon.**

mounting point, whereas the UE was placed in a street canyon, i.e., the Pasaje Chinitas, at distances of 15 m or 20 m from the IRS, depending on the specific test. Importantly, a building completely obstructed the direct LOS between the BS and UE, creating an authentic scenario where the HELIOS IRS acts as the only means of establishing a reflected communication path. Thus, the goal of this trial was to evaluate the reflector's ability to create virtual-line-of-sight (VLOS) connectivity by redirecting mmWave signals from the BS to the UE. To ensure effective redirection, the BS and UE antenna arrays were mechanically aligned so that the IRS was in their respective boresight. Multiple HELIOS variants were tested, specifically IRSs #1, #2, and #4, each showing different reflection beam characteristics as detailed in Sec. IV-A. Because of their different designs, the BS position and the IRS mounting orientation were adjusted for each setup to achieve the desired incidence and reflection behavior, e.g., by rotating the nodes on the mounting pole. In all configurations, the incident azimuth angle at the IRS was kept around $\phi_{in} = -45°$, whereas the reflected beam was aimed toward central azimuth angles $\phi_{out}$ of either 0° or 30°. Since all nodes were mounted at the same height of 1.5 m, the elevation angles for both incident EM wave and its reflection are at $\theta_{in} = \theta_{out} = 0°$.

To ensure high temporal consistency and repeatability in measurements, a magnetically mounted IRS holder was used. This allowed smooth transitions between IRS-enabled and IRS-disabled states with minimal disruption, enabling direct system performance comparisons under each condition. The UE was connected to a mobile workstation running a professional-grade wireless network analysis tool [91], which recorded a broad range of channel and link-layer metrics (i.e., more than 500 parameters) during continuous downlink (DL) transmission. The network was fully loaded with a 6 Gbit/s user datagram protocol (UDP) stream from the core network (CN) to the UE, ensuring the radio link operated under sustained high-throughput conditions and that dynamic beam management mechanisms remained actively engaged.

To evaluate the impact of the HELIOS IRSs on mmWave communication performance, we focused on a set of key metrics that collectively capture signal strength, link quality,

beam management behavior, and end-user throughput. These include the reference signal received power (RSRP), which quantifies the power of the received reference signal and reflects the effective signal strength; the reference signal strength indicator (RSSI), which provides a broader measure of received power inclusive of noise and interference; and the beam index (ID), which reveals how the mmWave communication system's beamforming algorithm adapts in response to IRS-induced path availability. In addition, the transmit power of the UE is monitored to assess whether IRS support enables more efficient power use, and the rank indicator, which indicates the number of spatial streams the system is able to exploit and is thus a crucial factor for MIMO performance. Lastly, throughput and block error rate (BLER) metrics were measured as direct indicators of link performance and robustness from the end-user perspective.

These metrics were collected over a continuous time window surrounding the IRS switch event. The mean, minimum, and maximum values of each parameter within a temporal interval that captures both steady-state behavior and transitional effects are evaluated accordingly. Unlike prior studies conducted under E-UTRAN / New Radio Dual Connectivity (EN-DC)-based FR2 connectivity, this trial was conducted entirely on an SA mmWave network, allowing the standalone performance of the FR2 link to be studied without sub-6 GHz anchoring [24], [92]. Moreover, the relatively high received signal levels ensured that the primary purpose of the HELIOS IRS was not to extend basic coverage, but rather to enhance the quality and resilience of the connection. This includes reducing power consumption, providing secondary propagation paths for increased robustness against blockage, and enabling additional spatial streams to increase throughput in the context of MIMO transmission [65, Ch. 5].

Fig. 17 shows the antenna pattern hull of the mmWave BS's antenna array in the azimuth-elevation plane, overlaid with gain contours for 32 predefined beams along with their respective indices. The antenna gain is represented with a color scale with four colors spanning the range from the approximate peak gain of 24 dBi (dark red) to gains $\leq$ 18 dB (deep blue). This discrete coloring scheme clearly highlights the main lobes of each beam and shows how all beams together form a grid of partially overlapping lobes, i.e., with no deep fades, that covers a wide angular space of about $20° \times 90°$.

Owing to the measurement setup, the central boresight region (azimuth and elevation angle of 0°) is of particular importance since this is the direction at which the IRSs under test are mounted. Hence, the two beams with IDs {#15, #20} are spatially aligned and are thus the most likely candidates for optimal signal enhancement. In contrast, beams with high azimuth angle magnitude, e.g. {#31, #47, #4, #36}, are expected to be used when no IRS is installed because they constitute NLOS paths, either through the building penetration or natural ambient reflection paths from buildings of the city square.

Furthermore, it is worth noting that, in conjunction with the 27.3 GHz carrier frequency and 29.7 cm IRS panel dimensions, the distances employed between IRS and UE, 15 m and 20 m, are slightly smaller or larger than the Fraunhofer distance $d_F = (2/\lambda) \cdot (29.7\,\text{cm})^2 = 16.07\,\text{m}$ [54], which marks a key transition distance between NF and FF propagation. Considering that the IRSs were custom-tailored to exhibit the desired reflection behavior in the infinite FF (cf. Sec. IV-A), and that our lab measurements yielded that the NF performance differs from the FF, better performance is expected for the 20 m IRS-to-UE setting. This limitation of FF-centric IRS configurations can be addressed by using a NF-extended reflection model along with the proposed design process from Sec. III-A, as shown in [89].

Last, it is acknowledged that the measurements are conducted in an essentially static environment, i.e., the UE is stationary and no pedestrians traverse through the measurement

**TABLE 9. Urban measurement setup and communication system details.**

| | Parameter | Description/Value |
|---|---|---|
| mmWave BS | Radio Unit | Nokia AWGUC AirScale |
| | Frequency Band | 5G band n258 (27.1–27.5 GHz, mmWave/FR2) |
| | Component Carriers | 4× 100 MHz using 120 kHz subcarrier spacing (SCS) |
| | Antenna Array | 12×16, cross-polarized, up to approx. 24 dBi gain |
| | Transmit Power | max. 34 dBm (approx. 2.5 W) without antenna gain |
| | MCS | 64-QAM (MCS index table 1) |
| | TDD | UL/DL slot ratio: 1/4 |
| | Capabilities | Release 16, NR standalone (FR2-only), 2×2 MIMO |
| Commercial UE | Device Model | Quectel 5GDM01EK + RG530F-EU |
| | Modem | Qualcomm SDX65 |
| | Antennas | Qualcomm RA530T + 4x QTM547 (8×8, cross-polarized) |
| | Power Class | Class 1 (max. 35 dBm / approx. 3.2 W) |
| | Capabilities | Release 16, 2×2 MIMO in FR2 |
| | Carrier Aggregation | off, i.e., uses only 100 MHz bandwidth |
| IRSs under Test | Measured IRSs | HELIOS #1, #2, and #4, cf. Sec. IV-A |
| | Az. Incidence Angle | $\phi_{in} = -45°$ |
| | Az. Reflection Angle | $\phi_{out} = \phi_{o,c} = 0°$ (IRS #1, #2) *or* 30° (IRS #4) |
| | Reflection Beamwidth | $\Delta\phi_o = 3°$ (IRS #1) *or* 10° (IRS #2, #4), $\Delta\theta_o = 3°$ |
| | Horizontal Distances | $d_{in} = 10\,\text{m}$ (BS-IRS), $d_{out} = \{15\,\text{m}, 20\,\text{m}\}$ (IRS-UE) |
| | Fraunhofer distance | $d_F = 16.08\,\text{m}$, i.e., best performance for $d_{out} \geq d_F$ (FF) |
| | Mounting Height | 1.5 m (Center of IRS Panel and BS/UE antenna arrays) |
| | | Hence, elevation angles: $\theta_{in} = 0°$, $\theta_{out} = \theta_{o,c} = 0°$ |
| Measurements | UE-side Measurements | Multi-Gbit/s DL UDP Traffic exceeding Link Capacity |
| | Time Resolution | Channel and Link Metrics available every 0.5 s |
| | Performance Metrics | NR SpCell: RSRP*, Beam Index*, RSSI, SINR |
| | | NR: TX Power, Rank Indicator |
| | | NR MAC DL: Throughput, BLER |
| | | NR PDSCH: MCS CW0 Index Distribution |

*Not just for *serving beam* but also for any further *detected beams* of the BS.

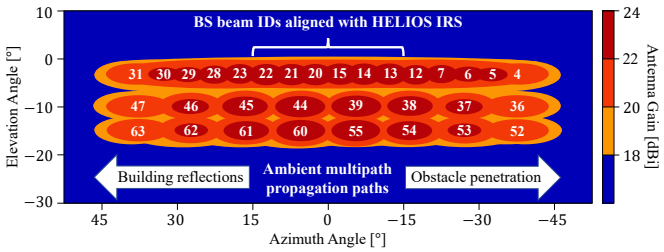


**FIGURE 17. Sketch of antenna pattern hull over 32 traffic beams of mmWave BS along with spatially matched beam indices. Owing to boresight placement of the IRSs under test, i.e., at azimuth and elevation angles of 0°, utilization of beams #15 or #20 is expected if it is mounted.**

area. Against this background, follow-up field trials in Málaga, Spain, will demonstrate that the horizontally broadened beam enhances connectivity throughout the entire confined corridor while ensuring smooth performance under UE mobility, thereby confirming effects observed in indoor trials [41], [78]. Since all communication nodes are deployed at low altitude (cf. Fig. 16), ambient pedestrian mobility would be likely to obstruct the direct IRS-to-UE sub-channel and introduce additional path loss of approximately 10 dB to 20 dB [93]. Nevertheless, strong indirect propagation paths between IRS and UE, e.g., through building reflections, may remain available due to the broad reflection beam. Future 6G network planning should nonetheless not only identify suitable IRS mounting positions for sustainable coverage extension [56], [94], but also explicitly account for ambient mobility to ensure resilient coverage. In this context, placing the IRS at a higher position near the entrance of the urban canyon could enable serving the UE from above, largely independent of pedestrian blockage. Future trials will thus feature IRSs with more complex combinations of azimuth and elevation angles of incidence and departure.

### *E. Field Performance of HELIOS IRS in Urban Scenario*

To assess the real-world impact of the proposed passive HELIOS reflectors on mmWave communication in urban environments, we systematically measured and analyzed both signal- and link-level performance indicators across various IRS deployments. The evaluation uses two complementary representations of the same measurement dataset: Tab. 10 shows the observed mean power characteristics of the DL-heavy communications along with the BS utilization, whereas Tab. 11 elaborates on peak changes of key link-level metrics, including throughput, signal to interference plus noise ratio (SINR), MCS, and BLER. The entries of these tables were extracted from the raw measurement time series, such as the ones for IRS #1 depicted in Fig. 18 for the metrics beam ID, DL RSRP, uplink (UL) TX power, and medium access control (MAC) layer DL BLER. Therein, it can be clearly seen that within the initial 40 s, the mmWave propagation conditions with the IRS positioned at 20 m distance from the UE are much more favorable than in the subsequent 40 s without the static-passive HELIOS IRS. Against this background, this article subsequently discusses mean and peak differences in the connectivity with and without IRS deployment.

The power-related performance improvements induced by HELIOS are summarized in Tab. 10. At a 20 m IRS-UE distance, HELIOS IRSs #1 and #4 show the highest RSRP improvements of about 9.9 dB and 9.7 dB, respectively, whereas HELIOS #1 shows a moderate gain of 5.8 dB. When the distance is reduced to 15 m, HELIOS #1 reaches a power gain of 10.0 dB, indicating strong performance in the NF-FF transition zone of the mmWave channel. These improvements are also reflected in RSSI, with power gains exceeding 8 dB for several configurations. In parallel, the IRSs also enable reduced UL transmit power from the UE by up to 10.1 dB. It is important to note that the TX power savings in the low-utilized UL correspond well with the highly-utilized DL RX power improvements. However, it is unknown whether there was also a BS side transmit power change depending on the IRS mounting state. All in all, these findings nonetheless show that IRSs not only improve the link budgets of the mobile equipment but also enable more energy-efficient transmissions for them, which corroborates recent research results [78].

Another key aspect shown in Tab. 10 is the behavior of beam index assignments. Without the IRS, the BS often switches among multiple serving and fallback beams, mainly beams #31 and #47, to maintain a good link. For example, with HELIOS #1 at 20 m, the serving beam switches between IDs #31, #47, and #52 when the IRS is not mounted. With the IRS, however, a stable beam, usually aligned with the new beam IDs #15, #16, #20, or #21, is chosen, indicating that the IRS creates a strong artificial propagation path (cf. beam ID time series in Fig. 18). This confirms the results from an external field trial in a similar public setting wherein the link was also stabilized by the IRS [17].

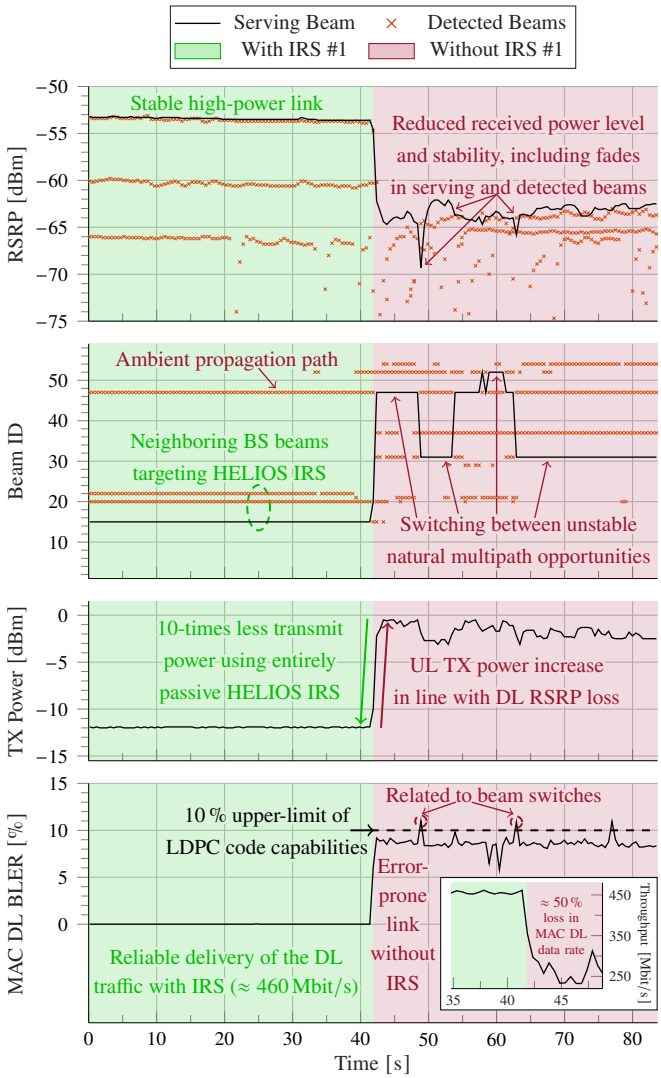


**FIGURE 18. mmWave connectivity in street canyon over time with clear negative impact of removing the entirely passive HELIOS IRS #1.**

**TABLE 10. Mean power characteristics of UE link *with* and *without IRSs* highlight their positive impact of up to 20 dB over both link directions. The observed effect arises from a novel introduced propagation path: in NLOS (without IRS), the serving BS beam is unstable based on weak ambient propagation paths, while beyond-LOS operation (with IRS) enables use of a single fixed beam along a previously infeasible steering direction.**

| IRS-UE Distance $d_{out}$ | | 20 m (UE in FF of FF IRS) | | | 15 m (UE in NF of FF IRS) | |
|---|---|---|---|---|---|---|
| **Mean Performance Metric** | | **HELIOS #1** | **HELIOS #2** | **HELIOS #4** | **HELIOS #1** | **HELIOS #2** |
| RSRP [dBm] (DL metric) | With IRS | −53.4 | −53.7 | −50.7 | −50.5 | −54.7 |
| | Without IRS | −63.3 | −58.9 | −60.4 | −60.5 | −61.6 |
| | ***RX Power Improvement*** | **9.9** | **5.3** | **9.7** | **10.0** | **6.8** |
| RSSI [dBm] (DL metric) | With IRS | −27.9 | −28.8 | −23.9 | −25.3 | −29.7 |
| | Without IRS | −37.0 | −32.9 | −34.2 | −34.1 | −35.3 |
| | ***Cross-validated RX Power Improvement*** | **9.2** | **4.1** | **10.3** | **8.8** | **5.6** |
| Transmit Power [dBm] (UL metric) | With IRS | −11.9 | −11.7 | −14.8 | −15.1 | −10.9 |
| | Without IRS | −1.8 | −6.1 | −5.2 | −5.2 | −3.7 |
| | ***TX Power Reduction*** | **10.1** | **5.6** | **9.6** | **9.9** | **7.2** |
| Beam Index with IRS (*Beam Switch*) | Fixed Serving Beam | $15^{r}$ | $20^{r}$ | $21^{r}$ | $15^{r}$ | $20^{r}$ |
| | Detected Beams | $\{20^{r}, 22^{r}, \underline{47}^{a}\}$ | $\{15^{r}, 20^{r}, \underline{31}^{a}, \underline{47}^{a}, 52^{a}\}$ | $\{\underline{5}^{a}, 20^{r}, 52^{a}\}$ | $\{13^{r}, 20^{r}, 21^{r}, \underline{31}^{a}, 47^{a}, 52^{a}\}$ | $\{15^{r}, 44^{r}, \underline{47}^{a}\}$ |
| Beam Index without IRS (*Beam Switch*) | Utilized Serving Beam(s) | $\{31^{a}, \underline{47}^{a}, 52^{a}\}$ | $\underline{47}^{a}$ | $\{4^{a}, \underline{5}^{a}, 37^{a}\}$ | $\{5^{a}, \underline{31}^{a}\}$ | $\{36^{a}, 37^{a}, \underline{47}^{a}\}$ |
| | Further Detected Beams | $\{37^{a}, 54^{a}\}$ | $\{\underline{31}^{a}, 37^{a}\}$ | $36^{a}$ | $\{6^{a}, 36^{a}, 37^{a}, 46^{a}, 54^{a}\}$ | $\{12^{a}, 46^{a}\}$ |

Approx. 10 dB impact of custom IRS on the UE side power metrics in downlink and uplink direction, respectively

UE side reporting on the detected and utilized BS beams underlines IRS-enabled enrichment of the ambient multipath propagation environment

Classification of BS beam orientation (cf. Fig. 17): $ID^{r}$: Reflector-based propagation path. $ID^{a}$: Ambient multipath propagation. $\underline{ID}$: Feasible beam regardless of IRS availability.

Fig. 17 supports this assessment by mapping the beam indices of the BS to the azimuth-elevation angular space. Beams #31, #47, and #52, which are used without the IRS, are at the edge of the antenna field of view; their main lobe directions can either be mapped to the propagation path penetrating the urban buildings or toward ambient buildings on the Plaza de la Constitución in order to use a natural reflection into the street canyon. With IRS #1, the beam IDs #31, #47, and #52 are used instead. These are near the boresight of the BS antenna array, which was mechanically aligned to the IRS. Hence, it can be confirmed that the introduced IRSs are automatically adopted by existing mmWave beam management between BS and UE nodes. Moreover, this recapitulates our finding that IRSs can be used not only for coverage extension or signal strength improvement, but also to improve serving beam stability in field deployments.

Both Tab. 10 and Fig. 18 outline that the RSRP is very high when compared to the minimum supported UE side RSRP level of approximately −105 dBm, which was identified in [10]. Hence, it is no surprise that the rank indicator metric is always, i.e., even without IRS, at the maximum supported value of 2. Considering the previous paragraph, this corroborates the findings from Sec. IV-C that the newly introduced propagation paths support both polarizations. This is because the UE's antenna array only supports one beam direction at a time, along which two data streams can be handled due to different polarizations. Moreover, this shows that our considered urban IRS use case is not about coverage extension but about attaining better spectral efficiency, energy efficiency, and link robustness within existing, NLOS-affected mmWave cell coverage.

Tab. 11 complements the signal-level findings by examining peak observed link-level performance indicators under similar conditions. Across all investigated HELIOS variants tested, significant improvements in SINR, with gains up to 9.9 dB at 20 m and 8.9 dB at 15 m can be observed. These SINR improvements lead directly to better communications efficiency, which may be noticed by applications in the form of increased DL throughput because higher MCS are utilized and BLER is reduced. For instance, HELIOS #1 at 20 m achieves a peak throughput of 478.2 Mbit/s, a major improvement over the baseline without the IRS at 274.4 Mbit/s. Modulation and coding statistics also show more aggressive transmission schemes with IRS support: Mean physical downlink shared channel (PDSCH) MCS levels are consistently higher with the IRS, reaching up to 23.8 (24 corresponds to 64-QAM with 75.4 % code rate) compared to baseline values in the 12 to 20 range (12 corresponds to 16-QAM with 42.4 % code rate) [95, Tab. 5.1.3.1-1]. Similarly, the BLER remains low, i.e., at or below 1 % in most cases with mounted IRS, whereas without IRS it is often as high as it is tolerable for a current cellular network, i.e., at 10 % owing to low-density parity-check (LDPC) code capabilities [96, Ch. 8.5.1]. It is worth highlighting the fact that the IRSs under test consistently lowered the BLER compared to the IRS-free baseline. Overall, these measurement results align well with our prior findings, confirming the availability of a novel propagation path that outshines prior NLOS propagation paths. Against this background, it is a key takeaway that the observed performance gains are not at the cost of reduced reliability in package delivery.

Overall, the measurement results contained in the two tables empirically confirm the benefits of entirely passive IRS deployments for efficient mmWave communications. The HELIOS reflectors provide strong gains in received power, link stability, and throughput, even in challenging NLOS scenarios. The improvements support the previously presented design principles established through EM simulations and near-field trials, confirming the role of HELIOS reflectors as a key enabler of practical, energy-efficient, high-throughput

**TABLE 11. Peak impact of proposed HELIOS IRSs on mmWave channel and link performance metrics for DL traffic, relative to the baseline.**

| IRS-UE Distance $d_{out}$ | | 20 m | | | 15 m | |
|---|---|---|---|---|---|---|
| **Peak Performance Metric** | | **IRS #1** | **IRS #2** | **IRS #4** | **IRS #1** | **IRS #2** |
| RSRP [dBm] (DL metric) | With IRS | −53.2 | −52.9 | −50.4 | −50.1 | −54.0 |
| | Without IRS | −69.3 | −70.5 | −63.9 | −67.4 | −64.5 |
| ***Delta: up to 17.6 dB*** | | 16.1 | **17.6** | 13.5 | 17.3 | 10.5 |
| RSSI [dBm] (DL metric) | With IRS | −27.6 | −28.0 | −23.3 | −24.7 | −28.7 |
| | Without IRS | −39.3 | −38.8 | −39.7 | −37.0 | −38.6 |
| ***Delta: up to 16.4 dB*** | | 11.7 | 10.8 | **16.4** | 12.3 | 9.9 |
| Transmit Power [dBm] (UL metric) | With IRS | −12.0 | −13.1 | −15.0 | −15.2 | −11.7 |
| | Without IRS | −0.5 | −1.0 | −1.7 | −3.7 | −1.8 |
| ***Delta: up to 13.3 dB*** | | 11.5 | 12.1 | **13.3** | 11.5 | 9.9 |
| SINR [dB] (DL metric) | With IRS | 29.0 | 28.4 | 30.4 | 30.3 | 28.4 |
| | Without IRS | 19.1 | 24.4 | 26.2 | 21.4 | 23.5 |
| ***Delta: up to 9.9 dB*** | | **9.9** | 4.0 | 4.2 | 8.9 | 4.9 |
| MAC DL Throughput [Mbit/s] | With IRS | 478.2 | 449.7 | 469.2 | 461.9 | 447.9 |
| | Without IRS | 203.5 | 208.7 | 312.2 | 337.5 | 278.6 |
| ***Delta: up to 275 Mbit/s*** | | **274.4** | 241.0 | 157.0 | 124.4 | 169.3 |
| Mean PDSCH MCS Index (DL metric) | With IRS | 23.8 | 23.5 | 23.8 | 23.6 | 23.4 |
| | Without IRS | 14.1 | 12.5 | 18.1 | 19.6 | 15.9 |
| ***Delta: up to 11 indices*** | | 9.7 | **11.1** | 5.8 | 4.0 | 7.5 |
| MAC DL BLER [%] | With IRS | 0.0 | 0.0 | 0.0 | 0.0 | 0.0 |
| | Without IRS | 11.0 | 9.3 | 9.2 | 9.1 | 9.6 |
| ***Delta: up to 11.0 perc. pts.*** | | **11.0** | 9.3 | 9.2 | 9.1 | 9.6 |

mmWave communications in urban settings.

The attained connectivity gains of the HELIOS reflectors, that were designed and manufactured for this article, are briefly compared with other static IRSs in exactly the same measurement setup, cf. [73, Tabs. 2–3]. It is noted that IRSs {#1, #2} from the 15 m IRS-to-UE distance setup are denoted by {*F*, *E*} in [73], and subsequently compared to four other reflectors {*A*, *B*, *C*, *D*}. Considering previously identified dynamic link and channel parameter behavior without a mounted IRS, this brief performance comparison focuses on the DL RSRP, DL SINR, MAC DL throughput, and the UL TX power metrics for the case that an IRS is mounted. It is found that the two HELIOS reflectors attain the highest peak throughputs, which are up to about 75 Mbit/s higher than the other four reflectors under test. This is corroborated by the highest SINR for HELIOS #2 (*Ref. F*). However, comparing the SINR metric has little relevance as there is only about 2 dB difference between IRS #2 and the worst-performing reflector. Differences between maximum RSRP and minimum TX power parameters are more pronounced: Whereas *Ref. B* attains the highest RSRP, the second highest is provided by HELIOS #2 (*Ref. F*). Similarly, the second-lowest minimum UE transmit power is attained by HELIOS #2. The 9 dB power deltas against *Ref. B* are reasonable considering that the HELIOS panel exhibits a 57 % smaller area plus a much broader reflection beam, cf. [73, Tab. 1]. Furthermore, considering the highest throughput (+75 Mbit/s), RSRP (+3 dB), and SINR (+2 dB) along with the lowest TX power (-3 dB) against similar-sized IRSs exhibiting narrower reflection beams (*Refs.* {*A, C, D*}), the geometry-driven HELIOS IRS – customized according to our contribution in Sec. III – is deemed more than competitive to other static IRS concepts.

## V. CONCLUSIONS AND OUTLOOK

This work was driven by the vision of enabling efficient future 6G radio access networks through the use of customized static reflecting geometries to systematically enhance mmWave connectivity in NLOS regions. In this context, the article focused on the HELIOS IRS architecture, which features a modular 3D-printed design that offers key advantages including low cost, zero power consumption, and scalable size. Building on this foundation, we summarize the key contributions below.

The literature review revealed a gap in existing IRS beam customization approaches, particularly in methods capable of simultaneously providing coverage across a predefined broad angular range and ensuring a guaranteed minimum in-beam RCS. To address this challenge, this article presented a holistic solution combining genetic algorithms with an far-field reflection model for beam shaping aimed at maximizing in-beam gain, and followed by an IRS size and module arrangement optimization to match it with the target value. Our sensitivity analysis, conducted across more than 1,000 HELIOS IRS design iterations, demonstrated that the proposed customization approach consistently achieved beam shapes within 5 dB to 9 dB of the unattainable theoretical upper limit, regardless of utilized IRS size and beamwidth. Furthermore, it outperformed the brute-force method in both computational efficiency and achievable guaranteed in-beam RCS. Against this dataset, we then validated that sensible panel size and module arrangements are determined successfully.

While much of the existing research on IRS concepts remains focused on theoretical and simulation-based studies, this article sought to complement this by custom-tailoring four HELIOS IRSs using the proposed framework. Through extensive experimental evaluations, the real-world performance of the customized IRSs was assessed under both controlled and realistic deployment conditions: First, evaluation in a laboratory setup showed that the near-field performance matched expectations from EM simulations, but differed from the far-field model-based design characteristics, because the measurement distance was short owing to size constraints of the anechoic chamber. Nonetheless, good signal integrity properties were observed at the preset directions, whereas the specular reflection was suppressed by up to 27.1 dB. The IRSs were then also evaluated in an urban testbed utilizing commercial mmWave BS and UE devices. We found that the IRSs enabled the mmWave communication system's beam management to leverage the newly introduced propagation path to increase mean DL RSRP and decrease mean UL TX power by up to 10.1 dB compared to the NLOS link state. Moreover, the IRS-assisted link was found to be more stable in terms of power and signal quality metrics, thus allowing for higher throughputs as a consequence of both lower BLER and higher MCS. Our investigation, complemented by comparisons against external (static and reconfigurable) IRSs designs that were also tested in these two European testbeds, further highlights the competitive performance of the HELIOS IRS architecture.

Future work will remain committed to making 6G smart radio environments a reality, by focusing on machine learning-assisted network planning that facilitates the systematic placement of customized IRSs in the deployment scenario [55], [56], [94]. The proposed HELIOS design approach may undergo refinements in this context, such as incorporating additional geometry parameters or supporting arbitrarily-shaped to multi-armed reflections for improved efficiency. Furthermore, our recent research on a near-field-extended reflection model will facilitate closer placement of the IRS to the UE service region [89].

## APPENDIX

### A. Sustainability Aspects of the HELIOS IRS Concept

This section provides details on the low-cost claim for the considered entirely passive IRS architecture, and discusses how the production concept, consisting of 3D-printing and spray-coating stages, can procure durable IRSs suitable for long-term operation under harsh outdoor conditions.

**Price Estimate:** The four reflector prototypes employed in Sec. IV were additively manufactured using low-cost PLA filament (approx. 23 € per spool) and subsequently conductively spray-coated with low-cost varnish (approx. 67 € per can) [20]. This leads to *material costs* for the HELIOS IRSs (30 cm × 30 cm) in the tens of Euros range. Conversely, synthetic static IRSs can be expected to be much more expensive per piece, i.e., within the hundreds of Euros range, due to printed circuit board (PCB)-based manufacturing material costs scaling with by panel size, substrate material (and thus, frequency), number of unit cells (and thus, frequency), and minimum order quantities. Naturally, both IRS architectures (geometry-based and synthetic) also incur manual labor costs during manufacturing, e.g., for assembly and quality insurance. Moreover, the following costs have to be accounted for, among other factors, in order to determine the *product price*: the depreciation costs associated with the 3D-printer and the paint booth, the expenses for consumable materials and scrap cost, the storage space and time for drying, the use of high-end branded products, the network planning and reflector optimization-related service costs (cf. Sec. III-A), the development costs, as well as the gross margin and taxes. Considering the reduced material costs of the proposed geometry-based IRS architecture, lower capital expenditure values are feasible compared to commercial synthetic mmWave IRSs: For example, custom-tailored static reflectors are typically priced at ≫1,000 € per piece, whereas reconfigurable IRSs (i.e., RISs) for research purposes at ≫10,000 € per piece while also incurring operational expenditures through continuous power consumption of up to a few tens of Watts, cf. [10, Tab. 1]. To put these capital and operational expenditures in context, commercial Open RAN mmWave radio units are characterized by high costs of ≫25,000 € per piece along with deployment-specific installation costs for mounting and wiring, while also consuming hundreds of Watts during operation [97, Tab. 6.5.2-2]. Against this background, dual cost benefits are attained if radio units are substituted by one or few entirely passive IRSs [55]. Hence, the claim that HELIOS is a low-cost solution, delivering high value-add for the network operator within the scope of the 6G IRS vision, is justified.

**Longevity and Robustness:** The employed prototypes consisting of PLA and conductive varnish are not suitable for long-term outdoor use, contrary to the implicit suggestion in Sec. IV. Reasons for this include insufficient thermal stability, which leads to partial surface warping and, consequently, undesirable changes in reflection behavior. Against this background, we identified the need for modifications in future field studies. Within systematic lab studies, the combination of ASA filament with two layers of coating (conductive bottom layer and acrylic top layer) was found to yield the following effects: First, ASA filament demonstrates superior heat resistance over PLA, PET, and PETG, exceeding extreme outdoor temperatures worldwide for dark materials exposed to direct midday summer sun. We observed form stability up to 90 °C over numerous heating-cooling cycles. Moreover, ASA also shows minimal degradation under UV radiation compared to other common 3D-printing filaments, indicating strong suitability for long-term outdoor applications. Second, ASA exhibits high resistance to moisture and oils, the latter being relevant for indoor factory (InF) use cases, with no visible or tactile changes after prolonged exposure, compared to PLA. This also holds in combination with the two varnishes, while also leading to no observable oxidation effects or similar. Furthermore, this combination increases mechanical robustness such that surface damage from brushing or scratching, e.g., from nearby vegetation during strong winds, is notably reduced without loss of reflectivity. Overall, this threefold material-coating configuration enables stable reflection characteristics in long-term public outdoor or private industrial deployments.

### B. Performance under Misaligned Conditions

This section studies additional reflection characteristics of preconfigured HELIOS IRSs, which were designed for a predetermined angular reflection space $\Omega_{out}$, constituting a set of azimuth and elevation angles of departure $(\phi_{out}, \theta_{out})$ spanning the horizontal and vertical beamwidths $\Delta\phi_{out}, \Delta\theta_{out}$. In particular, the installation may occur in a slightly different environment, e.g., due to an inaccurate site plan or mounting tolerances. Hence, the reflection beam could be misaligned by $\Delta\psi$, which may lead to performance loss for edge users.

**Methodology:** In the planned reflection beam area $\Delta\theta_{out} \times \Delta\phi_{out}$, the minimum in-beam RCS $\sigma^*$ is achieved per definition, cf. Sec. III-A. It is assumed that, in the worst-case, the reflection beam is $\Delta\psi$ too small in either direction, i.e., horizontally left and right as well as vertically up and down. The minimum in-beam RCS $\sigma^*_{BMA}(\Delta\psi)$ is therefore ascertained over the symmetrically enlarged reflection beam area $(\Delta\theta_{out} + 2\Delta\psi) \times (\Delta\phi_{out} + 2\Delta\psi)$ to determine the reflection beam misalignment (BMA)-based loss $L_{BMA}(\Delta\psi) = \sigma^* - \sigma^*_{BMA}(\Delta\psi)$. The empirical assessment is based on the 25 *symmetry*-based reflector designs with

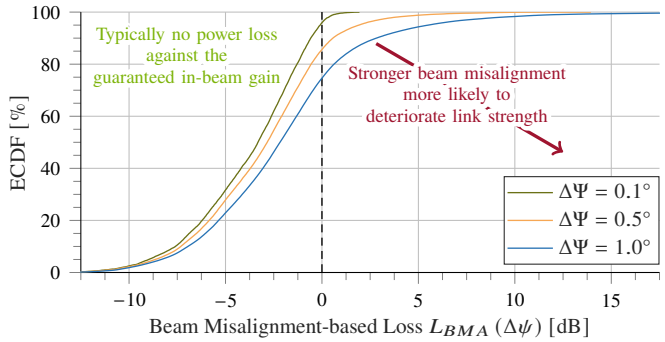


**FIGURE 19. The stronger the reflection beam misalignment $\Delta\Psi$ from erroneous installation or planning, the higher the risk that UEs at the edge of the reflection beam are served with reduced link strength.**

optimal $M \times N$ module arrangement for the target reflection beamwidths of 1° to 25°, cf. case study #1 in Sec. III-B. $\Delta\psi$ is an integer multiple of the therein employed angular design resolution $\Delta\phi_{o,res} = \Delta\theta_{o,res} = 0.1°$. Hence, $\Delta\psi = 0.1°$ represents a low misalignment, $\Delta\psi = 0.5°$ matches the value in [39], whereas $\Delta\psi = 1.0°$ constitutes a strong misalignment.

**Evaluation:** The empirical cumulative distribution function (ECDF) of incurred loss for the given BMAs are depicted in Fig. 19. It can be seen that for a low BMA $\Delta\Psi$, there is typically no loss (i.e., $L_{BMA} \leq 0$ dB) as the custom-tailored beam tends to be slightly broader than necessary because the optimization target is maximization of the minimum in-beam RCS value without penalizing out-of-beam RCS, cf. Fig. 7d and Fig. 9 in Sec. III-B. When increasing the beam misalignment, the likelihood to incur loss increases, e.g., to 25.4 % for 1° BMA. This leads to, for example, a 10 % chance that a 2.9 dB loss against the targeted common in-beam performance is incurred.

**Mitigation Strategies:** Against this background, however, it should be emphasized that it is likely in practice that the pre-deployment network planning jointly determines the position and coverage of static IRSs such that they overlap slightly with the coverage of other IRSs and BSs to achieve a consistent connectivity level [56]. Therefore, even if a misaligned reflection beam results in undesired loss along this propagation path, it does not mean that end-to-end performance losses have to occur. Last, it is noted that BMA-based losses can be avoided proactively by custom-tailoring the reflection beam for a slightly larger service area than required, using $2\Delta\psi$-broader horizontal and vertical beamwidths, because this leads to a comparatively low beam broadening-based loss that reduces $\sigma^*$, cf. Eq. (18) and Fig. 7b in Sec. III-B.

## ACKNOWLEDGMENT

The authors would like to thank Yasin Gümüs for his support in validating the proposed HELIOS IRS design process in Sec. III, and Marcel Kaudewitz for assisting in the development and testing of robust HELIOS IRSs for long-term operation in challenging environments, given in the Appendix.

## REFERENCES

[1] M. Alsabah *et al.*, "6G wireless communications networks: A comprehensive survey," *IEEE Access*, vol. 9, pp. 148 191–148 243, Nov. 2021, DOI: 10.1109/ACCESS.2021.3124812.

[2] Z. Cui, P. Zhang, and S. Pollin, "6G wireless communications in 7 GHz to 24 GHz band: Opportunities, techniques, and challenges," in *Proc. IEEE DySPAN Symp.*, May 2025, DOI: 10.1109/DySPAN64764.2025.11115934.

[3] M. Na *et al.*, "Operator's perspective on 6G: 6G services, vision, and spectrum," *IEEE Commun. Mag.*, vol. 62, no. 8, pp. 178–184, Aug. 2024, DOI: 10.1109/MCOM.001.2400060.

[4] M. Morini, E. Moro, C. Rubaltelli, I. Filippini, A. Capone, and D. De Donno, "Exploring upper-6 GHz and mmWave in urban 5G networks: A direct on-field comparison," *IEEE Trans. Mobile Comput.*, vol. 24, no. 12, pp. 13 034–13 047, Dec. 2025, DOI: 10.1109/TMC.2025.3587904.

[5] M. Danger, C. Arendt, H. Schippers, S. Böcker, N. Beckmann, R. Schmitt, and C. Wietfeld, "6G industrial networks: Mobility-centric evaluation of multi-cell mmWave systems," in *Proc. IEEE VTC-Spring Conf.*, Jun. 2025, DOI: 10.1109/VTC2025-Spring65109.2025.11174718.

[6] D. Shakya, S. Ju, O. Kanhere, H. Poddar, Y. Xing, and T. S. Rappaport, "Radio propagation measurements and statistical channel models for outdoor urban microcells in open squares and streets at 142, 73, and 28 GHz," *IEEE Trans. Antennas Propag.*, vol. 72, no. 4, pp. 3580–3595, Apr. 2024, DOI: 10.1109/TAP.2024.3366581.

[7] J. Ko *et al.*, "Millimeter-wave channel measurements and analysis for statistical spatial channel model in in-building and urban environments at 28 GHz," *IEEE Trans. Wirel. Commun.*, vol. 16, no. 9, pp. 5853–5868, Sep. 2017, DOI: 10.1109/TWC.2017.2716924.

[8] A. Ramírez-Arroyo *et al.*, "FR2 5G networks for industrial scenarios: Experimental characterization and beam management procedures in operational conditions," *IEEE Trans. Veh. Technol.*, vol. 73, no. 9, pp. 13 513–13 525, Sep. 2024, DOI: 10.1109/TVT.2024.3393533.

[9] M. Di Renzo, F. H. Danufane, and S. Tretyakov, "Communication models for reconfigurable intelligent surfaces: From surface electromagnetics to wireless networks optimization," *Proc. IEEE*, vol. 110, no. 9, pp. 1164–1209, Sep. 2022.

[10] S. Häger, M. Kaudewitz, F. Schmickmann, S. Böcker, and C. Wietfeld, "Field performance evaluation of a mechatronic reflector system in a private mmWave network environment," *IEEE Open J. Commun. Soc.*, pp. 5005–5029, Jun. 2025, DOI: 10.1109/OJCOMS.2025.3572723.

[11] B. Imaz-Lueje, E. Martinez-de-Rioja, and M. Arrebola, "Design of electromagnetic skins based on multi-faceted reflectarrays for millimeter-wave coverage improvement," in *Proc. EuCAP Conf.*, Apr. 2025, DOI: 10.23919/EuCAP63536.2025.10999305, IEEE.

[12] W. Ni, A. Zheng, W. Wang, D. Niyato, N. Al-Dhahir, and M. Debbah, "From single to multi-functional RIS: Architecture, key technologies, challenges, and applications," *IEEE Netw.*, vol. 39, no. 1, pp. 38–46, Jan. 2025, DOI: 10.1109/MNET.2024.3481028.

[13] W. Tang *et al.*, "Wireless communications with reconfigurable intelligent surface: Path loss modeling and experimental measurement," *IEEE Trans. Wirel. Commun.*, vol. 20, no. 1, pp. 421–439, Jan. 2021, DOI: 10.1109/TWC.2020.3024887.

[14] Z. Zhang *et al.*, "Active RIS vs. passive RIS: Which will prevail in 6G?" *IEEE Trans. Commun.*, vol. 71, no. 3, pp. 1707–1725, Mar. 2023, DOI: 10.1109/TCOMM.2022.3231893.

[15] X. Yuan, Y.-J. A. Zhang, Y. Shi, W. Yan, and H. Liu, "Reconfigurable-intelligent-surface empowered wireless communications: Challenges and opportunities," *IEEE Wirel. Commun.*, vol. 28, no. 2, pp. 136–143, Apr. 2021, DOI: 10.1109/MWC.001.2000256.

[16] Z. Zhang and L. Dai, "Reconfigurable intelligent surfaces for 6G: Nine fundamental issues and one critical problem," *Tsinghua Sci. Technol.*, vol. 28, no. 5, pp. 929–939, Oct. 2023, DOI: 10.26599/TST.2023.9010001, IEEE.

[17] A. Shokair *et al.*, "Real world field trial for RIS-aided commercial 5G mmWave wireless communication," in *Proc. EuCNC/6G Summit*, Jun.

2024, IEEE. DOI: 10.1109/EuCNC/6GSummit60053.2024.10597120.

[18] R. Liu, J. Dou, P. Li, J. Wu, and Y. Cui, "Simulation and field trial results of reconfigurable intelligent surfaces in 5G networks," *IEEE Access*, vol. 10, pp. 122 786–122 795, Nov. 2022, DOI: 10.1109/ACCESS.2022.3223447.

[19] H. Yang *et al.*, "Beyond limitations of 5G with RIS: Field trial in a commercial network, recent advances, and future directions," *IEEE Commun. Mag.*, vol. 62, no. 10, pp. 132–138, Oct. 2024, DOI: 10.1109/MCOM.024.2300440.

[20] S. Häger, K. Heimann, S. Böcker, and C. Wietfeld, "Holistic enlightening of blackspots with passive tailorable reflecting surfaces for efficient urban mmWave networks," *IEEE Access*, vol. 11, pp. 39 318–39 332, Apr. 2023, DOI: 10.1109/ACCESS.2023.3267676.

[21] K. Goto, S. Suyama, T. Yamada, K. Arai, and O. Kagaya, "Experimental trials with combination of multiple transmissive metasurfaces and beamforming for mmW coverage enhancement," in *Proc. IEEE VTC-Fall Conf.*, Oct. 2023, DOI: 10.1109/VTC2023-Fall60731.2023.10333724.

[22] D. Kitayama, D. Kurita, K. Miyachi, Y. Kishiyama, S. Itoh, and T. Tachizawa, "5G radio access experiments on coverage expansion using metasurface reflector at 28 GHz," in *Proc. IEEE APMC Conf.*, Dec. 2019, DOI: 10.1109/APMC46564.2019.9038267.

[23] A. Benoni, F. Capra, M. Salucci, and A. Massa, "Toward real-world indoor smart electromagnetic environments – a large-scale experimental demonstration," *IEEE Trans. Antennas Propag.*, vol. 71, no. 11, pp. 8450–8463, Nov. 2023, DOI: 10.1109/TAP.2023.3305053.

[24] M. Danger, C. Arendt, H. Schippers, S. Böcker, M. Mühleisen, P. Becker, J. B. Caro, G. Gjorgjievska, M. A. Latif, J. Ansari, N. Beckmann, N. König, R. Schmitt, and C. Wietfeld, "Performance evaluation of IRS-enhanced mmWave connectivity for 6G industrial networks," in *Proc. IEEE M&N Symp.*, Jul. 2024, DOI: 10.1109/MN60932.2024.10615534. Best Paper Young Author Award.

[25] E. Björnson and Ö. T. Demir, *Introduction to Multiple Antenna Communications and Reconfigurable Surfaces*. Hanover, MA, USA: Now Publishers, Jan. 2024, ISBN: 978-1-63828-315-7.

[26] J. An *et al.*, "Codebook-based solutions for reconfigurable intelligent surfaces and their open challenges," *IEEE Wirel. Commun.*, vol. 31, no. 2, pp. 134–141, Apr. 2024, DOI: 10.1109/MWC.010.2200312.

[27] J. An, M. Debbah, T. J. Cui, Z. N. Chen, and C. Yuen, "Emerging technologies in intelligent metasurfaces: Shaping the future of wireless communications," *IEEE Trans. Antennas Propag.*, pp. 1–18, May 2025, DOI: 10.1109/TAP.2025.3571069. Early access.

[28] E. Martini and S. Maci, "Theory, analysis, and design of metasurfaces for smart radio environments," *Proc. IEEE*, vol. 110, no. 9, pp. 1227–1243, Sep. 2022, DOI: 10.1109/JPROC.2022.3171921.

[29] G. Oliveri, F. Zardi, L. Tosi, and A. Massa, "On the use of specular reflecting passive EM skins in NLOS wireless backhauling – performance and design guidelines," *IEEE Trans. Antennas Propag.*, vol. 72, no. 10, pp. 7893–7904, Oct. 2024, DOI: 10.1109/TAP.2024.3438940.

[30] A. P. Ganesh, W. Khawaja, O. Ozdemir, I. Güvenç, H. Nomoto, and Y. Ide, "Propagation measurements and coverage analysis for mmWave and sub-THz frequency bands with transparent reflectors," in *Proc. IEEE VTC-Spring Conf.*, Aug. 2023, DOI: 10.1109/VTC2023-Spring57618.2023.10200244.

[31] Z. Zhakipov, M. Makin, A. Nasser, A. Abdallah, A. Celik, and A. M. Eltawil, "From lab to digital twin: Calibration of mmWave ray-tracing with RIS reflections," in *Proc. IEEE PIMRC Symp.*, Sep. 2025, DOI: 10.1109/PIMRC62392.2025.11275011.

[32] A. F. Vaquero, E. Martinez-de-Rioja, M. Arrebola, J. A. Encinar, and M. Achour, "Smart electromagnetic skin to enhance near-field coverage in mm-Wave 5G indoor scenarios," *IEEE Trans. Antennas Propag.*, vol. 72, no. 5, pp. 4311–4326, May 2024, DOI: 10.1109/TAP.2024.3383216.

[33] TMY Technology Inc., "XRifle reflector," Tech. Rep. [Online]. Available: https://tmytek.com/products/components/xrifle

[34] Dai Nippon Printing Co., Ltd., "Reflect array for 5G," Tech. Rep. [Online]. Available: https://www.global.dnp/biz/solution/products/detail/10161719_4130.html

[35] Nissha Co., Ltd., "Metasurface reflectarray," Tech. Rep. [Online]. Available: https://connect.nissha.com/filmdevice/en/metasurface_antenna

[36] N. A. Abbasi *et al.*, "Ultra-wideband double directional channel measurements for THz communications in urban environments," in *Proc. IEEE ICC Conf.*, Jun. 2021, DOI: 10.1109/ICC42927.2021.9500510.

[37] W. Khawaja, O. Ozdemir, Y. Yapici, F. Erden, and I. Güvenç, "Coverage enhancement for NLOS mmWave links using passive reflectors," *IEEE Open J. Commun. Soc.*, vol. 1, pp. 263–281, Jan. 2020, DOI: 10.1109/OJCOMS.2020.2969751.

[38] X. Wei, W. Mei, Q. Wu, B. Ning, and Z. Chen, "Movable antennas meet intelligent reflecting surface: When do we need movable antennas?" in *Proc. IEEE WCNC Conf.*, Mar. 2025, DOI: 10.1109/WCNC61545.2025.10978634.

[39] J. Ferreira, A. Leßmann, C. N. Manchón, and D. Schreurs, "End-to-end experimental validation of RIS and passive reflectors in mmWave 5G systems," *IEEE Trans. Antennas Propag.*, 2026, submitted.

[40] Z. Li, O. A. Topal, Ö. T. Demir, E. Björnson, and C. Cavdar, "Mixed static and reconfigurable metasurface deployment in indoor dense spaces: How much reconfigurability is needed?" in *Proc. IEEE WCNC Conf.*, Apr. 2024, DOI: 10.1109/WCNC57260.2024.10570594.

[41] M. Danger, S. Häger, C. Arendt, F. Schmickmann, M. Kaudewitz, S. Böcker, and C. Wietfeld, "Reflection instead of densification: Experimental insights into IRS-aided industrial 6G mmWave," 2026, submitted for review. Demo video: https://tiny.cc/ICCDanger.

[42] S. Häger, M. Danger, K. Heimann, Y. Gümüs, S. Böcker, and C. Wietfeld, "Custom design and experimental evaluation of passive reflectors for mmWave private networks," in *Proc. IEEE LANMAN Symp.*, Jul. 2024, DOI: 10.1109/LANMAN61958.2024.10621891. Best Paper Award.

[43] N. Torkzaban, M. A. Khojastepour, M. Farajzadeh-Tehrani, and J. S. Baras, "RIS-aided mmWave beam-forming for two-way communications of multiple pairs," *ITU Journal on Future and Evolving Technologies*, vol. 4, no. 91, pp. 87–101, Mar. 2023, DOI: 10.52953/VBEX2484.

[44] F. Pepe, I. Iudice, G. Castaldi, M. Di Renzo, and V. Galdi, "A study of cylindrical reconfigurable intelligent surfaces," in *Proc. Metamaterials Congress*, Sep. 2025, DOI: 10.1109/Metamaterials65622.2025.11174223. IEEE.

[45] M. Al Hajj, K. Tahkoubit, H. Shaiek, V. Guillet, and D. L. Ruyet, "On beam widening for RIS-assisted communications using genetic algorithms," in *Proc. EuCNC/6G Summit Conf.*, Jun. 2023, DOI: 10.1109/EuCNC/6GSummit58263.2023.10188311. IEEE.

[46] S. Prabh, "On intelligent reflecting surfaces element allocation using genetic algorithms," in *Proc. IEEE PIMRC Symp.*, Sep. 2022, DOI: 10.1109/PIMRC54779.2022.9977607.

[47] G. Encinas-Lago, A. Albanese, V. Sciancalepore, X. Costa-Pérez, A. Banchs, and D.-T. Phan-Huy, "A cost-effective RISs deployment to abate the coverage problem in B5G networks," *IEEE Trans. Wirel. Commun.*, vol. 23, no. 10, pp. 15 276–15 290, Oct. 2024, DOI: 10.1109/TWC.2024.3428338.

[48] B. K. Daniel and A. L. Anderson, "Phase-only beam broadening of contiguous uniform subarrayed arrays," *IEEE Trans. Aerosp. Electron. Syst.*, vol. 56, no. 5, pp. 4001–4013, Oct. 2020, DOI: 10.1109/TAES.2020.2987115.

[49] L. Maman, S. Zach, and A. Boag, "Beam shaping by phase-only waveform encoding for transmitting array antennas in radar applications," *IEEE Open J. Antennas Propag.*, vol. 6, no. 2, pp. 478–486, Apr. 2025, DOI: 10.1109/OJAP.2025.3529505.

[50] J. Song, H. Zheng, and L. Zhang, "Application of particle swarm optimization algorithm and genetic algorithms in beam broadening of phased array antenna," in *Proc. ISSSE Symp.*, vol. 1, Sep. 2010, DOI:

10.1109/ISSSE.2010.5607063. IEEE.

[51] X. Liu *et al.*, "Terahertz beam steering using a MEMS-based reflectarray configured by a genetic algorithm," *IEEE Access*, vol. 10, pp. 84 458–84 472, Aug. 2022, DOI: 10.1109/ACCESS.2022.3197202.

[52] G. Oliveri, G. Gottardi, F. Zardi, and A. Massa, "On the synthesis of multibit reconfigurable passive skins for smart EM environments," *IEEE Antennas Wirel. Propag. Lett.*, vol. 23, no. 11, pp. 3774–3778, Nov. 2024, DOI: 10.1109/LAWP.2024.3428318.

[53] G. C. Karaova and Ö. Ergül, "Design, fabrication, and measurement of efficient beam-shaping reflectors for 5G applications," *IEEE Trans. Antennas Propag.*, vol. 70, no. 12, pp. 11 335–11 343, Dec. 2022, DOI: 10.1109/TAP.2022.3209279.

[54] S. Häger, S. Böcker, and C. Wietfeld, "Reflection modeling of modular passive IRS geometries," *IEEE Wirel. Commun. Lett.*, vol. 14, no. 5, pp. 1366–1370, May 2025, DOI: 10.1109/LWC.2025.3542564.

[55] S. Häger, M. Geis, K. Šabanović, P. Jörke, S. Böcker, and C. Wietfeld, "6G network design with custom-tailored IRSs for sustainable millimeter-wave connectivity enhancements in industrial environments," in *Proc. IEEE FNWF Conf.*, Nov. 2025, DOI: 10.1109/FNWF66845.2025.11317335. Demo video: https://tiny.cc/HELIOS-SRE.

[56] M. Geis, S. Häger, B. Krluku, and C. Wietfeld, "Hybrid active-passive network design enabled by physics-informed ML-based propagation modeling," in *Proc. IEEE INFOCOM Wkshps.*, May 2026, accepted. Available: https://comnets.etit.tu-dortmund.de/storages/cni-etit/r/Research/Publications/2026/Geis_2026_INFOCOM/Geis_INFOCOMWkshps_AuthorsVersion.pdf.

[57] Z. Jiang, X. Chen, J. Lyu, L. Fu, and R. Zhang, "Quasi-static IRS: 3D shaped beamforming for area coverage enhancement," in *Proc. IEEE GLOBECOM Conf.*, Dec. 2025, forthcoming. Available (DOI): 10.48550/arXiv.2505.01076.

[58] X. Teng *et al.*, "Arbitrary beam pattern synthesis and measurement for mmWave RIS with discrete phase shifts," *IEEE Trans. Veh. Technol.*, vol. 74, no. 6, pp. 9973–9978, Jun. 2025, DOI: 10.1109/TVT.2025.3540926.

[59] W. Wang, A. Doufexi, and M. A. Beach, "Integer-based pattern synthesis for asymmetric multi-reflection RIS," in *Proc. IEEE WCNC Conf.*, Apr. 2024, DOI: 10.1109/WCNC57260.2024.10571319.

[60] H. Al-Tous and O. Tirkkonen, "Coverage area optimized static reflecting surfaces," *IEEE Trans. Wirel. Commun.*, vol. 23, no. 8, pp. 9375–9388, Aug. 2024, DOI: 10.1109/TWC.2024.3362068.

[61] J. Fenn and M. Raskino, *Mastering the hype cycle*, ser. Gartner Inc./Harvard Business School Press. Boston, MA, USA: Harvard Business Review Press, Sep. 2008, ISBN: 978-1-42212-110-8.

[62] M. Monemi, M. Rasti, A. S. De Sena, M. A. Fallah, M. Latva-Aho, and M. Di Renzo, "Practical challenges for reliable RIS deployment in heterogeneous multi-operator multi-band networks," *IEEE Commun. Mag.*, vol. 63, no. 6, pp. 154–160, Jun. 2025, DOI: 10.1109/MCOM.002.2400441.

[63] F. Xu *et al.*, "Coordinating multiple intelligent reflecting surfaces without channel information," *IEEE Trans. Signal Process.*, vol. 72, pp. 31–46, Jan. 2024, DOI: 10.1109/TSP.2023.3334818.

[64] S. T. Shah *et al.*, "Coded environments: Data-driven indoor localisation with reconfigurable intelligent surfaces," *Nature Commun. Eng.*, vol. 3, no. 66, pp. 1–10, Apr. 2024, DOI: 10.1038/s44172-024-00209-0, Springer.

[65] European Telecommunications Standards Institute (ETSI), "Reconfigurable intelligent surfaces (RIS); use cases, deployment scenarios and requirements," GR 001 V1.2.1, Feb. 2025.

[66] ——, "Reconfigurable intelligent surfaces (RIS); communication models, channel models, channel estimation and evaluation methodology," GR 003 V1.2.1, Feb. 2025.

[67] ——, "Reconfigurable intelligent surfaces (RIS); implementation and practical considerations," GR 004 V1.1.1, Mar. 2025.

[68] S. Gadhai and R. Budhiraja, "Evolution of network nodes: From IAB to IRS," 3GPP Highlights Newsletter, no. 6, pp. 20–21, May 2023. [Online]. Available: https://www.3gpp.org/images/newsletters/3GPP_Highlights_Issue_6_opt.pdf

[69] A. A. Kherani and S. Kumar, "Reconfigurable intelligent surfaces: Standardization and testbed development in India," TSDSI Quarterly Newsletter, vol. 8, no. 44, Telecommunications Standards Development Society India (TDSI), Tech. Rep., Dec. 2024. [Online]. Available: https://tsdsi.in/wp-content/uploads/2020/09/Newsletter-Dec-2024-Webfile.pdf

[70] RIS Alliance, "Potential standardization work for reconfigurable intelligent surface," White Paper 1.0, Apr. 2025, DOI: 10.12142/FuTURE.202504003.

[71] J. Ferreira, A. Leßmann, D. Schreurs, and C. N. Manchón, "An empirical wideband performance analysis of mmWave passive RIS and reflectors," in *Proc. IEEE PIMRC Symp.*, Istanbul, Türkiye, Sep. 2025, DOI: 10.1109/PIMRC62392.2025.11275147.

[72] A. M. Toubal *et al.*, "OTA characterization of reconfigurable intelligent surface at 5G mmWave band," in *Proc. EuCNC/6G Summit Conf.*, Jun. 2025, DOI: 10.1109/EuCNC/6GSummit63408.2025.11037079. IEEE.

[73] J. Ferreira, A. Leßmann, D. Schreurs, and C. N. Manchón, "Passive reflectors for power-efficient 5G NR urban coverage: Field validation," 2026, submitted for review.

[74] X. Fu, R. Peng, G. Liu, J. Wang, W. Yuan, and M. Kadoch, "Channel modeling for RIS-assisted 6G communications," *MDPI Electronics*, vol. 11, no. 19, pp. 1–13, Sep. 2022, art. no. 2977. DOI: 10.3390/electronics11192977.

[75] Q. Xue *et al.*, "A survey of beam management for mmWave and THz communications towards 6G," *IEEE Commun. Surv. Tutor.*, vol. 26, no. 3, pp. 1520–1559, 2024, DOI: 10.1109/COMST.2024.3361991.

[76] G. C. Alexandropoulos, V. Jamali, R. Schober, and H. V. Poor, "Near-field hierarchical beam management for RIS-enabled millimeter wave multi-antenna systems," in *Proc. IEEE SAM Wkshp.*, Jun. 2022, DOI: 10.1109/SAM53842.2022.9827873.

[77] S. Zeng, H. Zhang, B. Di, Z. Han, and L. Song, "Reconfigurable intelligent surface (RIS) assisted wireless coverage extension: RIS orientation and location optimization," *IEEE Commun. Lett.*, vol. 25, no. 1, pp. 269–273, Jan. 2021, DOI: 10.1109/LCOMM.2020.3025345.

[78] M. Danger, M. Khalili, S. Böcker, and C. Wietfeld, "Improving energy efficiency of industrial mmWave connectivity with context-sensitive IRS support," in *Proc. IEEE PIMRC Symp.*, Sep. 2025, DOI: 10.1109/PIMRC62392.2025.11274884.

[79] N. U. Hassan, J. An, M. Di Renzo, M. Debbah, and C. Yuen, "Efficient beamforming and radiation pattern control using stacked intelligent metasurfaces," *IEEE Open J. Commun. Soc.*, vol. 5, pp. 599–611, Jan. 2024, DOI: 10.1109/OJCOMS.2023.3349155.

[80] D. E. Goldberg, *Genetic algorithms in search, optimization, and machine learning*. Boston, MA, USA: Addison-Wesley Publishing Comp., Inc., Jan. 1989, ISBN: 978-0-201-15767-3.

[81] J. Stoer and R. Bulirsch, *Introduction to numerical analysis*. New York, NY, USA: Springer, Apr. 2013, ISBN: 978-1-4757-5592-3.

[82] Ansys, Inc. High frequency simulation software (HFSS). [Online]. Available: https:/www.ansys.com/hfss

[83] K. Heimann, S. Häger, and C. Wietfeld, "Demo abstract: Experimental 6G research platform for digital twin-enabled beam management," in *Proc. ACM MobiWac Symp.*, Oct. 2023, DOI: 10.1145/3616390.3618282. Demo video: https://tiny.cc/HeliosDemonstrator.

[84] M. Magarotto, L. Schenato, M. Santagiustina, A. Galtarossa, and A.-D. Capobianco, "Plasma-based intelligent reflecting surface for beam-steering and polarization conversion," *IEEE Access*, vol. 11, pp. 43 546–43 556, May 2023, DOI: 10.1109/ACCESS.2023.3272569.

[85] H. Kim *et al.*, "RIS-enabled self-localization with FMCW radar," *IEEE Trans. Veh. Technol.*, vol. 74, no. 11, pp. 18 255 – 18 260, Nov. 2025,

DOI: 10.1109/TVT.2025.3580602.

[86] Keysight Technologies, Inc., "F9651A multi-probe compact antenna test range (CATR) chamber," Data Sheet, Feb. 2024. [Online]. Available: https://www.keysight.com/us/en/product/F9651A

[87] ——, "N5247B 4-port PNA-X network analyzer," Technical Specification, Jan. 2024. [Online]. Available: https://www.keysight.com/us/en/product/N5247B

[88] ——, "M9484C VXG signal generator," Data Sheet, Mar. 2025. [Online]. Available: https://www.keysight.com/us/en/product/M9484C

[89] S. Häger, M. Kaudewitz, and C. Wietfeld, "Near-field extension of analytical reflection model for large-scale mmWave IRS geometries in 6G," in *Proc. IEEE ICC Conf.*, May 2026, accepted. Available: https://comnets.etit.tu-dortmund.de/storages/cni-etit/r/Research/Publications/2026/Haeger_2026_ICC/Haeger_ICC_AuthorsVersion.pdf.

[90] 6G-SANDBOX Project. Pilot 6G site Málaga. [Online]. Available: https://6g-sandbox.eu/pilot-6g-sites/malaga

[91] Keysight Technologies, Inc., "Nemo Outdoor drive test solution," Brochure, Nov. 2024. [Online]. Available: https://www.keysight.com/us/en/product/NTA50000B

[92] M. Danger, S. Häger, K. Heimann, S. Böcker, and C. Wietfeld, "Empowering 6G industrial indoor networks: Hands-on evaluation of IRS-enabled multi-user mmWave connectivity," in *Proc. EuCNC/6G Summit Conf.*, Jun. 2024, DOI: 10.1109/EuCNC/6GSummit60053.2024.10597036. IEEE.

[93] M. Haferkamp, S. Häger, S. Böcker, and C. Wietfeld, "Machine learning-aided sensing in private mmWave networks for industrial applications," in *Proc. IEEE GLOBECOM Wkshps.*, Dec. 2024, DOI: 10.1109/GCWkshp64532.2024.11100825. [Online]. Available: https://github.com/tudo-cni/immerse_dataset

[94] M. Geis, S. Häger, and C. Wietfeld, "Taming mmWave connectivity prediction with DRaGon: AI propagation modeling for cluttered industrial environments," in *Proc. IEEE FNWF Conf.*, Nov. 2025, DOI: 10.1109/FNWF66845.2025.11317319. Second Place Best Paper Award.

[95] 3rd Generation Partnership Project (3GPP), "TSG RAN; NR; physical layer procedures for data (release 18)," Technical Specification (TS) 38.214, Sep. 2023, version 18.0.0.

[96] ——, "TSG RAN; NR; BS radio transmission and reception (release 18)," Technical Specification (TS) 38.133, Apr. 2025, version 19.0.0.

[97] Open RAN Alliance, "O-RAN WG use cases and overall architecture; network energy saving use cases," Technical Report, Jun. 2023, version 2.00, release 003. [Online]. Available: https://orandownloadsweb.azurewebsites.net/download?id=442

## BIOGRAPHIES

**Simon Häger** (Graduate Student Member, IEEE) received the M.Sc. degree in Communications Engineering from RWTH Aachen University, Aachen, Germany, in 2020, and the B.Sc. degree in Electrical Engineering from Paderborn University, Paderborn, Germany, in 2018. He is pursuing the Dr.-Ing. degree at TU Dortmund University, Dortmund, Germany, with a focus on efficient millimeter-wave communication systems utilizing custom-tailored passive reflectors. For instance, this research on IRS technologies was honored with the Best Paper Award at the IEEE LANMAN Symposium 2024. His work at the Chair of Communication Networks (ComNets) also investigates native channel-based positioning and sensing services of 5G/6G networks.

**João Ferreira** (Graduate Student Member, IEEE) received the M.Sc. degree in Electrotechnical engineering with a specialization in Telecommunications from the NOVA University of Lisbon, Lisbon, Portugal, in 2023. He is currently pursuing a Ph.D. degree in Electrical Engineering with KU Leuven and Keysight Technologies, Belgium. His research interests include IRS and UM-MIMO testing and performance assessment.

**Stefan Böcker** received his Dipl.-Ing. degree from TU Dortmund University, Dortmund, Germany, in 2013. He started as a Research Assistant at the Chair of Communication Networks (ComNets), TU Dortmund University. In 2016 he took over as the Chair's Head of the Research Group on 5G networks before being appointed Chief Engineer in 2021, where he is currently responsible for the coordination of third-party funded research activities. His main research interests are scalability in unlicensed frequency domains, 5G networks with a focus on mMTC, as well as operation of private networks in licensed domains with a special interest in industrial IoT environments.

**Dominique Schreurs** (Fellow, IEEE) received the M.Sc. degree in Electronic Engineering and the Ph.D. degree from the University of Leuven (KU Leuven), Leuven, Belgium, in 1992 and 1997, respectively. She is currently a Full Professor with KU Leuven, Leuven, Belgium, where she is also the Chair of the Leuven Center on Information and Communication Technology (Leuven ICT). She has been a Visiting Scientist with Agilent Technologies, Santa Rosa, CA, USA; ETH Zürich, Zürich, Switzerland; and the National Institute of Standards and Technology, Boulder, CO, USA. Her research interests include the microwave and millimeter-wave characterization and modeling of transistors, nonlinear circuits, aqueous liquids, and system design for wireless communications and biomedical applications. Prof. Schreurs served as the President for the IEEE Microwave Theory and Techniques Society from 2018 to 2019, and as the President for the ARFTG Organization from 2018 to 2019. She was the TPC Co-Chair of IMS 2023, the Editor-in-Chief of IEEE Transactions on Microwave Theory and Techniques, and an IEEE MTT-S Distinguished Microwave Lecturer.

**Christian Wietfeld** (Senior Member, IEEE) received the Dr.-Ing. and Dipl.-Ing. degrees from RWTH Aachen University, Aachen, Germany. He is currently a Full Professor and the Head of the Chair of Communication Networks (ComNets) at TU Dortmund University, Dortmund, Germany. For more than 30 years, he has been a Coordinator of and a Contributor to large-scale research projects on Internet-based mobile communication systems within both academia and industry at RWTH Aachen (1992–1997), Siemens AG (1997–2005), and TU Dortmund (2005 to date). His current research interests include the design and performance evaluation of 5G and 6G communication networks for cyber-physical systems in energy, transport, robotics, and emergency response. Prof. Wietfeld is the author of more than 400 peer-reviewed papers and holds several patents. He has been a Co-Founder of the IEEE Global Communications Conference Workshop on Wireless Networking for Unmanned Autonomous Vehicles and is a Member of the Technical Editor Board of the IEEE Wireless Communication Magazine. In addition to more than 15 IEEE Best Paper Awards, he was the recipient of the ITU-T Outstanding Contribution Award for his work on the standardization of next-generation mobile network architectures.